Supplement of Clim. Past, 21, 299–326, 2025
https://doi.org/10.5194/cp-21-299-2025-supplement

Climate of the Past
Open Access
EGU

Supplement of

Ice-proximal sea ice reconstruction in the Powell Basin, Antarctica, since the Last Interglacial

Wee Wei Khoo et al.

Correspondence to: Wee Wei Khoo (wee.wei.khoo@awi.de)

Supplement

S1: Age model

The age model of marine sediment core PS118_63-1 was first established using a comparative analysis of the XRF-Ti, magnetic susceptibility (MS), wet bulk density and total organic carbon (TOC) records against that of the EDML $\delta^{18}O$ record (Fig. S1). Glacial and/or cold periods (i.e., MIS 2-4, 5d and 6) within core PS118_63-1 were identified based on higher XRF-Ti, MS and density values, and lower TOC contents, while low/decreasing XRF-Ti, MS and density values with elevated TOC contents reflect the interglacial/warm periods (i.e., MIS 1 and 5e) in the core. Furthermore, the MIS 5/6 boundary is indicated by the biostratigraphic marker *Rouxia leventerae* (ca. 130 ka BP; Zielinski et al., 2002). Since <1% relative abundance of *Rouxia leventerae* was found at core depth 6.19 m (0.6%), we estimated the last occurrence of *Rouxia leventerae* to be around 6.2 m. Planktic foraminifera were also selected for AMS ^{14}C-dating (Table S1) using the Mini Carbon Dating System (MICADAS; Mollenhauer et al., 2021) at the Alfred Wegener Institute (AWI), Bremerhaven, Germany. The ^{14}C ages were calibrated to calendar ages using the PaleoDataView software (v0.9.5.25; Butzin et al., 2017; Heaton et al., 2020; Langner and Mulitza, 2019).

To further refine the age model within each glacial/interglacial interval, we considered additional age control tie points identified in records from a nearby marine core U1537 (MS, XRF-Fe and Opal) and the EDML ice core (ssNa+). See Fig. S2 for the tie points identified in the respective records of marine core PS118_63-1 with marine core U1537 and the EDML ice core. During the correlation analysis, multiple records from the same core were examined collectively to ensure that the age-depth ranges of respective tie points remained consistent across all records. The eventual tuning of records from core U1537 and EDML ice core with marine core PS118_63-1 was conducted using the QAnalyseries software (v1.5.1; Kotov and Pälike, 2018). A final comparison was then made between all the tie points identified from marine cores PS118_63-1 (XRF-Ti, Fe, MS, opal and $PIPSO_{25}$), U1537 (MS, XRF-Fe and opal) and EDML ice core ($\delta^{18}O$ and ssNa+). The most suited and/or fitting tie points were selected, while duplicates were rejected (as indicated by the black crosses in Fig. S1 and S2). A summary of the tie points used for the establishment of the age model of marine core PS118_63-1 is provided in Table S2. To account for age uncertainty, we adopted four age errors provided in the age model of core U1537 (refer to Supplementary Table 2 of Weber et al., 2022), and with them as reference, an age error of ±1 kyr was imposed for tie points between MIS 1 and 3, while ±2 kyr was prescribed for tie points from MIS 4-6 (Table S2). We also imposed an age error of ±1 kyr for the tie points derived from the EDML $\delta^{18}O$ record. Lastly, the Bayesian age-depth modeling was established using Bacon v2.5.8 (Blaauw and Christen, 2011) on RStudio v2022.07.02.

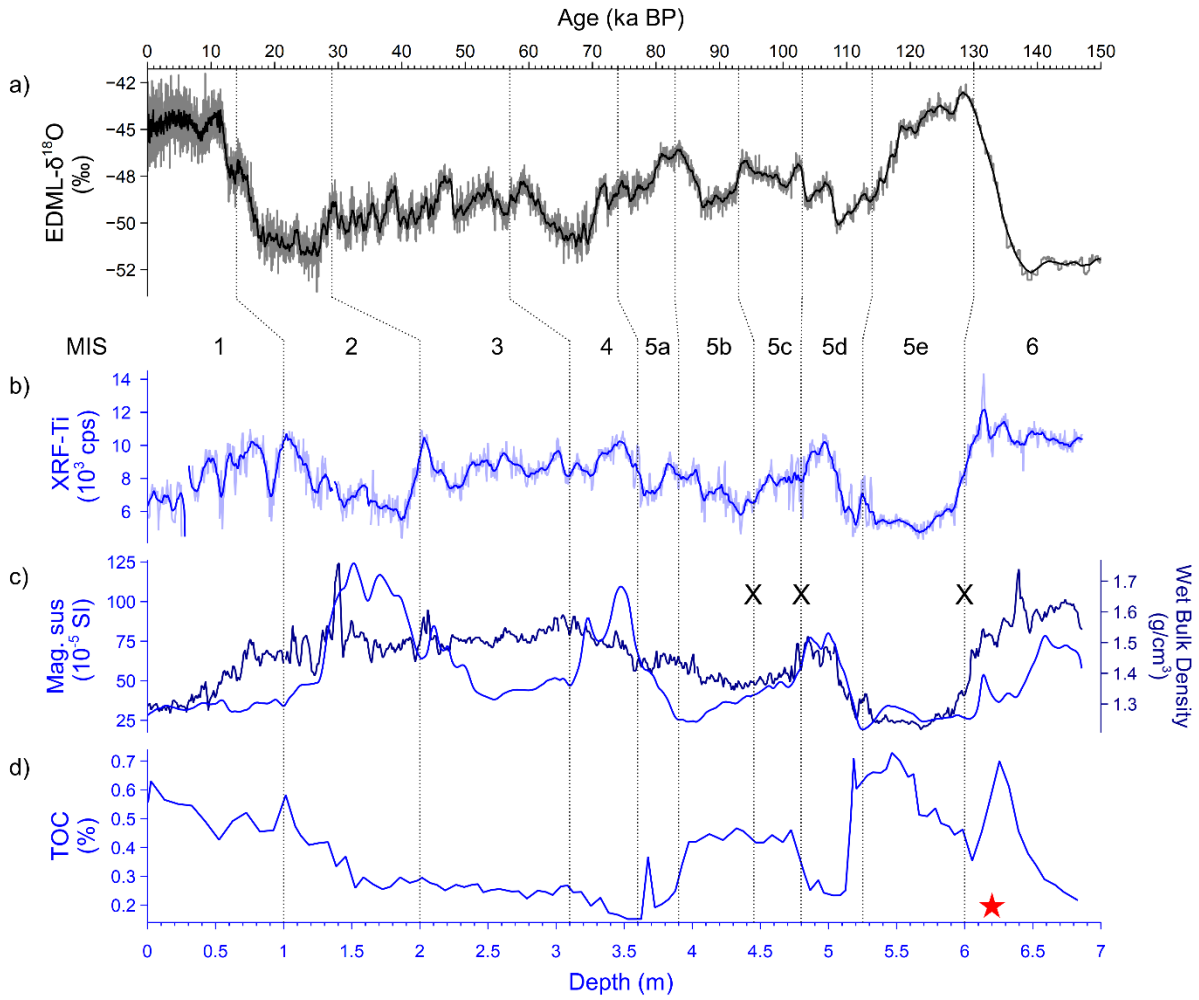

Figure S1. Age-depth comparison between the a) EDML $\delta^{18}O$ record against that of records, b) XRF-Ti, c) magnetic susceptibility, wet bulk density and d) TOC from marine sediment core PS118_63-1. Black crosses indicate tie points that were not chosen for use in the final age model after careful comparison between all age control tie points. Red star denotes the depth at which *R. leventerae*, a marker for MIS 5/6 boundary, has been identified. Age intervals for MIS 1-4 and 6 are in accordance to Lisiecki and Raymo (2005) and MIS 5 substages are referenced to Bianchi and Gersonde (2002).

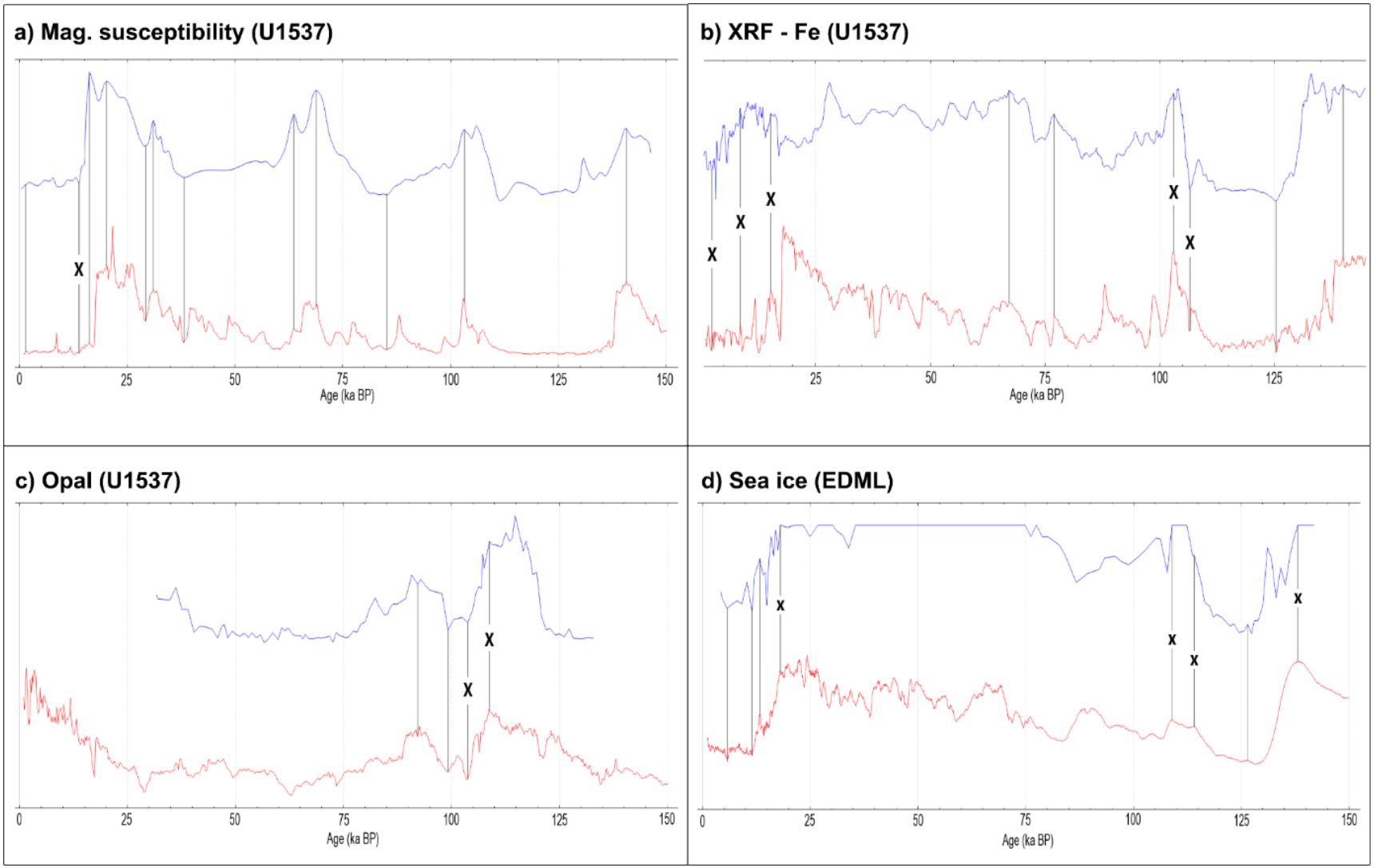

Figure S2. Plots of age control tie points identified in records a) magnetic susceptibility, b) XRF – Fe and c) opal records of marine core U1537 (red) against marine core PS118_63-1 (blue), and d) EDML ssNa+ record (red) against that of the $PIPSO_{25}$ record from marine core PS118_63-1 (blue). Black crosses indicate tie points that were not selected for inclusion in the final age model after careful comparison between all tie point records.

Table S1. Radiocarbon dates taken from marine sediment core PS118_63-1. Calendar and reservoir ages are in respect to IntCal20 as defined in the PaleoDataView software.

Sample Name	AWI Nr.	Material	$F^{14}C$ (abs)	^{14}C age (kyrs)	Cal age (ka BP)	Reservoir age (kyrs)
PS118_63-1_ 163-165cm	9742.1.1	*N. pachyderma*	0.1259 ±0.0025	16.647 ±0.158	17.603 ±0.935	2.216 ±0.287
PS118_63-1_ 179-181cm	9743.1.1	*N. pachyderma*	0.0845 ±0.0023	19.850 ±0.221	21.422 ±0.862	2.192 ±0.286

Table S2: Tie points used for age-depth model for marine sediment core PS118_63-1.

S/N	MIS	Depth (m)	Age (ka BP)	± Age (kyrs)	Tie point
1	1	0.076	1.2	1	U1537-MS
2	1	0.125	5.772	1	EDML-ssNa+
3	1	0.625	10.675	1	EDML-ssNa+
4	1	0.925	13.352	1	EDML-ssNa+
5	1	1	14	1	EDML-$\delta^{18}O$
6	2	1.516	16.2	1	U1537-MS
7	2	1.64	17.603	0.935^	^{14}C-dating
8	2	1.706	20	1	U1537-MS
9	2	1.8	21.422	0.862^	^{14}C-dating
10	3	2	29	1	EDML-$\delta^{18}O$
11	3	2.018	29.21	0.78*	U1537-MS
12	3	2.098	31.2	1	U1537-MS
13	3	2.548	38	1	U1537-MS
14	4	3.1	57	1	EDML-$\delta^{18}O$
15	4	3.228	63.64	2.28*	U1537-MS
16	4	3.46	67.2	2	U1537-Fe
17	4	3.478	68.8	2.1*	U1537-MS
18	5a	3.6	74	1	EDML-$\delta^{18}O$
19	5a	3.84	76.8	2	U1537-Fe
20	5b	3.9	83	1	EDML-$\delta^{18}O$
21	5b	4.028	85	2	U1537-MS
22	5b	4.33	92	2	U1537-Opal
23	5c	4.83	99.2	2	U1537-Opal
24	5d	4.868	103.17	1.71*	U1537-MS
25	5e	5.25	114	1	EDML-$\delta^{18}O$
26	5e	5.68	125.2	2	U1537-Fe
27	5e	5.83	126.336	2	EDML-ssNa+
28	6	6.2	130	2	*R. leventerae*
29	6	6.56	139.8	2	U1537-Fe
30	6	6.588	140.6	2	U1537-MS

^Age error taken from calibrated age uncertainty (refer to Table S1)

*Age error adopted from age model for marine core U1537 (refer to Supplementary Table 2 of Weber et al., 2022)

S2: ^{230}Th-excess constant-rate-of-supply model

To estimate the ^{230}Th-excess constant-rate-of-supply (CRS) age model for PS118_63-1, a total of 54 freeze-dried, ground and homogenized sediment samples were selected (at specific depth intervals) for the determination of uranium (U) and thorium (Th) isotopes (^{230}Th, ^{232}Th, ^{238}U and ^{234}U). The samples were first digested in a pressure-assisted microwave digestion system (CEM MarsXpress; 24 samples per batch). Following which, 15 mL of the digested solution underwent a separation and purification process via the seaFAST automatic column separation system, using TRU resin. Each Th/U fraction was then analyzed via sector-field inductively coupled plasma mass spectrometry (SF-ICP-MS Element2). U-isotopes were measured in low resolution using a cyclonic spray chamber, while Th-isotopes were measured with an Apex IR desolvation device for increasing ion yield, and in a custom-made resolution of R=2000 for increasing abundance sensitivity. The methods employed in the determination of ^{230}Th-excess and subsequent CRS-dating for PS118_63-1 are described in Geibert et al. (2019), with the calculation of the CRS age following a method by Appleby and Oldfield (1978).

The robustness of the age model for PS118_63-1 determined using 30 tie points (Table S2) is supported by the strong correlation between the tie points-derived age model and estimations via the ^{230}Th-excess CRS-dating approach (Fig. S3). The deviations are to be expected considering possible changes in focusing and the limited ^{230}Th-inventory considered in this core.

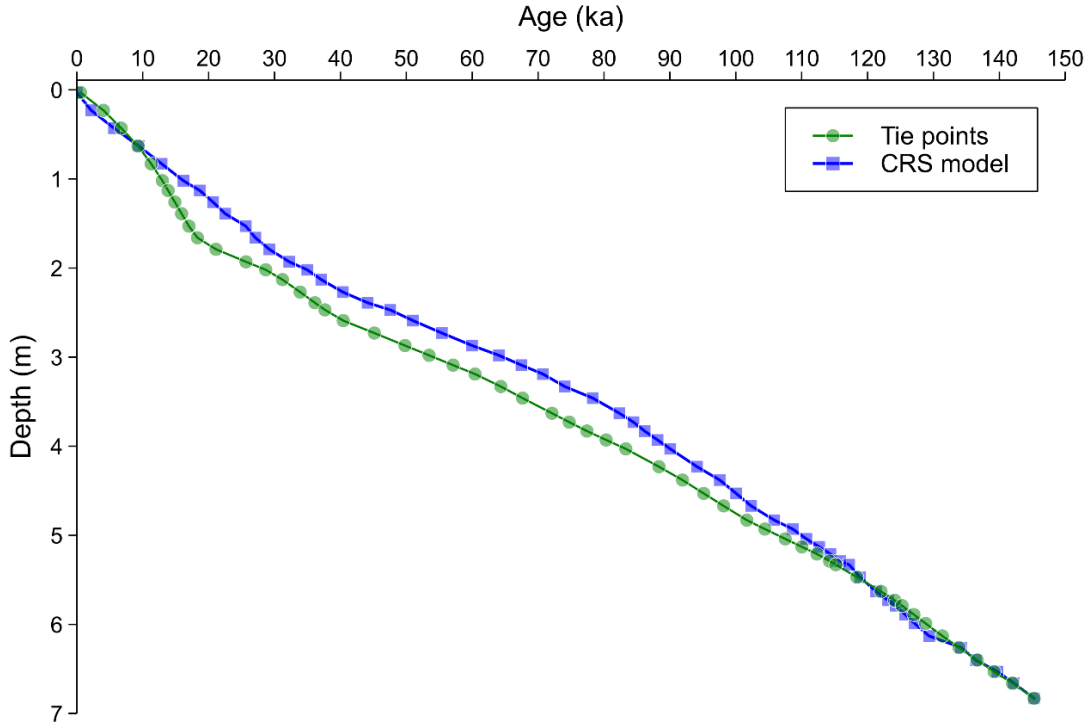

Figure S3. Comparison of age-depth profile of PS118_63-1 established based on tie points and ^{230}Th-excess CRS model.

S3: Numerical model and climate simulations

3.1 Community Earth System Models applications

The Community Earth System Models (COSMOS) have been successfully applied for the study of both colder and warmer than present climates – during, and beyond, the Cenozoic, both at orbital and tectonic time scales. In many cases, COSMOS has helped to improve our understanding of inferences from the geologic record. They have provided a dynamical framework of relevant processes in the climate system that may mechanistically explain reconstructed climate patterns. Examples for this work include simulations of the climates of the Cretaceous (Klages et al., 2020; Niezgodzki et al., 2019), of the Miocene (Hossain et al., 2020; 2021; Knorr and Lohmann, 2014; Knorr et al., 2011; Stein et al., 2016), of the Pliocene (Stepanek and Lohmann, 2012; Stepanek et al., 2020), of the Penultimate Glacial (Stein et al., 2017), of the LIG (Gierz et al., 2017; Pfeiffer and Lohmann, 2016; Stein et al., 2017), of the LGM (Zhang et al., 2013), and of the Holocene (Guagnin et al., 2016). Furthermore, the model has been employed towards a large number of process studies. Among these are the works by Knorr et al. (2021) on glacial termination, the study by Kaboth-Bahr et al. (2021) on the delay of Northern Hemisphere glaciation by Mediterranean heat injection into the North Atlantic Ocean during the Pliocene, the publication by Zhang et al. (2021) on the impact of astronomical forcing on Pleistocene millennial climate variability, and the investigation by Lohmann et al. (2022) on the potential contribution of increased vertical mixing towards reduced meridional temperature gradients in warm climates of the Pliocene and Miocene.

3.2 COSMOS-modeled climate states

The climate states *piControl*, *mh6k*, *lgm21k*, *lig125k*, and *pgm140k* are derived from equilibrium climate simulations, where we analyze the climate state at the end of a spin up. In these cases, COSMOS have been instantaneously exposed to reconstructions of greenhouse gases and of orbital forcing, and to paleogeography, if applicable. An exception to this methodology is the LIG climate state at 128 ka BP, derived from simulation *lig128k*. This simulation stems from the computation of a transient evolution of LIG climate from 130 ka BP to 115 ka BP, where the COSMOS have been employed with time-varying greenhouse gas concentrations and orbital forcing applying an acceleration of a factor of 10. The initial ocean state at 130 ka BP has been created to mirror conditions that are representative for the penultimate deglaciation, Termination II (TII; 140 – 130 ka BP). This ocean state has been created based on a weak hosing (0.05 Sv) under perpetual 130 ka BP forcing. To derive the climate conditions at 128 ka BP, we average the transient model climate state over the 100 model years that refer to the period from 128.5 ka BP to 127.5 ka BP. Details of the model setups of the various simulations are provided in Table S3.

3.3 Comparison of COSMOS with other climate models

There exists an extensive bibliographic record evaluating the performance of COSMOS, in comparison to other climate models including those in the context of the third and fourth phases of the Paleoclimate Modeling Intercomparison Project (PMIP3; Braconnot et al., 2012; PMIP4; Kageyama et al., 2017), which are part of the Climate Modeling Intercomparison Project (CMIP; Eyring et al., 2016). These studies span a wide range of time periods, including the Holocene (Varma et al., 2012; Dallmeyer et al., 2013; 2015), the Last Interglacial (Bakker et al., 2014; Jennings et al., 2015; Lunt et al., 2013), the Pliocene (Haywood et al., 2013; 2020), the Miocene (Burls et al., 2021), and the Eocene (Lunt et al., 2021). A key inference from these published works, relevant to our study, is that among the ensemble of PMIP3-class model simulations of the Southern Ocean, COSMOS, like some models, is known to project a relatively small warm bias in sea surface temperature (SST; see Fig. 4e and f in Lunt et al., 2013). This supports the use of said model in the study of sea ice and SST in the Weddell Sea region.

While the previously mentioned studies cover various aspects of COSMOS's modeled climate in comparison to simulations from other models, these studies provide no perfect match with regard to the time slices and variables considered in our study. Therefore, we provide additional comparison of our results with other PMIP models for those variables and time slices that are relevant to our study. Unfortunately, such an analysis is only possible in an incomplete manner. For instance, direct comparisons of the COSMOS-simulated sea ice and SST with data from the PMIP ensembles must focus on the pre-industrial (PI), mid-Holocene, and Last Glacial Maximum climate states. For the Penultimate Glacial Maximum (140 ka BP) and the two Last Interglacial time slices (128 ka BP and 125 ka BP) employed by us, no comparable PMIP simulations are available. In particular, PMIP3 does not cover any time slice for the Last Interglacial, while PMIP4 considers *lig127k* (127 ka BP) as one singular

time slice during the Last Interglacial (Otto-Bliesner et al., 2017), which is unfortunately out of sync with our Last Interglacial model simulations. Higher-tiered Last Interglacial simulations from PMIP4 (Otto-Bliesner et al., 2017) are as well not overlapping with our work. For reference, we will nevertheless undertake a comparison of our COSMOS data for the 128 and 125 ka BP time slices with the 127 ka BP time slice from the PMIP4 model. This will put our work into the context of recent modeling work on the Last Interglacial.

To facilitate a meaningful comparable model-to-model evaluation of our COSMOS data with results from other climate models in the broader paleoclimate modeling community, we assess our model data against all outputs from the CMIP5/PMIP3 and CMIP6/PMIP4 models available through the Earth System Grid Federation (ESGF; accessed via https://esgf-data.dkrz.de). A list of models used in the PMIP simulations, the search criteria employed during data retrieval, and data citations are provided in Table S4. All available data are also systemically selected and pertinent to the climate states under investigation in our study. They include: 1) PMIP3 and PMIP4 simulations *piControl* for a comparison with our PI climate state – here we focus on those models that provide at least one paleoclimate simulation, and other PI climate states are discarded from our analysis; 2) PMIP3 and PMIP4 simulations *mid-Holocene* for a comparison with our 6 ka BP climate state; 3) PMIP3 and PMIP4 simulations *lgm* for comparison with our 21 ka BP climate state; 4) PMIP4 simulation *lig127k* for a comparison with our 128 ka and 125 ka climate states. Our analyses were based on the last 100 model years of simulations, where available. Note that for some models or simulations, data for less than 100 model years have been published via ESGF. We downloaded monthly mean SST (tos) from both CMIP5/PMIP3 and CMIP6/PMIP4 ensembles, monthly mean sea-ice cover (sic) from the CMIP5/PMIP3 ensemble, and monthly mean sea-ice cover (siconc) from the CMIP6/PMIP4 ensemble. In general, data is represented as the monthly climatological mean.

Monthly mean data is unavailable for a small number of models. In such cases, we either computed the monthly mean from daily output or utilized climatological means directly provided by ESGF. Note that not all models provide all variables relevant to our study. Furthermore, inaccessibility of specific data nodes limited our utilization of the full PMIP ensemble. Consequently, we considered all data sets accessible, and this means that ensemble means of sea-ice cover and SST from one specific simulation may not necessarily cover the same models. Models providing at least one relevant dataset are highlighted in Table S5.

3.4 PMIP3 and PMIP4 models outputs: An evaluation against COSMOS model findings

In this section, we present the simulated spring/summer (NDJFMA) and winter (ASO) sea-ice cover, and summer (DJF) and winter (JJA) SST results from PMIP3 and PMIP4 models, subject to data availability. The modeled time slices cover the PI, 6, 21 ka BP for PMIP3 and PI, 6, 21 and 127 ka BP for PMIP4. All PMIP ensemble data has been remapped to match the grid used in the COSMOS. For each specific time slice, and CMIP generation, we computed ensemble means and standard deviation of the population (σ_n; for brevity, referred to as σ from here on). Agreement between COSMOS and PMIP3/PMIP4 models results is evaluated based on a 2σ threshold criterion. Results derived from COSMOS are considered as agreeing with the PMIP data if they are within the 2σ range of the ensemble.

3.4.1 Simulated sea-ice cover from PMIP3 and PMIP4 models

Figures S4 and S5 provide simulated spring/summer and winter sea-ice cover plots, considering ensemble means, σ and agreement within 2σ threshold between COSMOS and PMIP3 for three time slices (21, 6 ka BP and PI). Corresponding PMIP4 ensemble means, σ, and comparison with COSMOS are shown for the same time slices in Fig. S6.2-4 and S7.2-4. Likewise, panels a and b of Fig. S6.1 and S7.1 display the ensemble means and σ simulated by PMIP4 model for 127 ka BP. Figures S6.1c and S7.1c compare PMIP4 127 ka BP simulation results to COSMOS outputs from 128 ka BP, while Fig. S6.1d and S7.1d show the level of agreement with COSMOS simulation at 125 ka BP. We observe that the PMIP3/PMIP4 ensemble σ for both the spring/summer and winter seasons are appreciable. The ensemble σ of sea-ice cover during spring/summer is notably higher close to the Antarctic Peninsula and along coastal areas (Fig. S4b and S6b). Whilst, for winter sea-ice cover, the PMIP3/PMIP4 models exhibit more pronounced ensemble uncertainty farther away from the continent, increasing towards the edges of the sea-ice extent (Fig. S5b and S7b). Comparison of sea-ice data, COSMOS vs. PMIP3, shows agreement within the 2σ threshold criterion at our study sites (Fig. S4c and S5c). However, larger regions of disagreement (>2σ threshold) are observed when comparing sea-ice cover in COSMOS to results from PMIP4 (Fig. S6c and S7c). For both PMIP3 and PMIP4, there is wider distribution of disagreement along the 50ºS latitude for the 21 ka BP time slice, while smaller disagreements for PI

and 6 ka BP are observed near to the edge of the sea-ice extent. Note that simulated winter sea-ice conditions at Site PS118_63-1 agree between COSMOS and PMIP4 across PI, 6 and 21 ka BP. For 21 ka BP, agreement regarding winter sea ice is given for locations of both sites. Only in the case of PMIP4, the winter sea ice for PI and 6 ka BP time slices, as well as the spring/summer sea ice of PI, 6 and 21 ka BP time slices, study sites are outside (but in several cases close to) regions where the 2σ threshold criterion is fulfilled. From these findings, we infer that the COSMOS model generally produces a denser, and in many regions more extensive sea-ice cover compared to PMIP3 and (PMIP4) ensemble models. While at core sites, agreement with PMIP model ensembles is more frequent. Disagreements, when they occur, are biased towards the PMIP4 model, the winter season, and the 21 ka BP. In general, we observe a higher degree of disagreement for simulated sea-ice cover at core site PS67/219-1, which is often closer to the sea ice margin than core site PS118_63-1.

3.4.2 Simulated sea surface temperature from PMIP3 and PMIP4 models

Similarly, the ensemble means, σ and COSMOS-PMIP3 models agreement (within 2σ threshold) for the simulated summer and winter SST plots for the three same time slices are presented in Fig. S8 and S9, while those obtained using the PMIP4 model (PI, 6, 21 and 127 ka BP time slices) are provided in Fig. S10 and S11. Both PMIP3- and PMIP4-derived SST plots show considerable ensemble σ around the 40-50ºS latitude, especially off the coast of the eastern South American continent (refer to panel b of Fig. S8 to S11). Furthermore, a distinctly lower ensemble σ is observed in the Weddell Sea for the winter SST data (Fig. S9b and S11b). On the model-to-model agreement between COSMOS and PMIP, as with our sea ice simulations, we note higher alignment of our SST results with PMIP3 than with PMIP4, particularly at our study sites. For the comparison with PMIP3, the SST at our study sites is well outside the regions of model discord. In the case of PMIP4, agreement is larger for the winter season, with no overlap of regions of disagreement at study site PS118_63-1 and either no or mild overlap with study site PS67/219-1. Beyond the study site, similar to sea-ice cover, we notice greater model-to-model disagreement for the 21 ka BP time slice compared to the PI and 6 ka BP time slices. It is also worth noting that the SST model-to-model discord is greater in regions not covered by sea ice. For example, in Fig. S9, areas with particularly low PMIP3 ensemble σ, such as the Weddell Sea, tend to exhibit higher simulated winter sea-ice cover as seen in Fig. S5. Similarly, in Fig. S8, regions with greater uncertainty in summer SST in the Weddell Sea correspond to smaller sea-ice cover (Fig. S4).

3.4.3 Evaluation of COSMOS in comparison to PMIP models

In our assessment of the degree of agreement between COSMOS and PMIP3 simulations based on a 2σ threshold criterion, we observe generally good model-to-model agreement for both sea-ice cover and SST. The most significant discordance occurs close to, or north of, the sea ice border (15% isoline; see panel c in Fig. S4 and S5, S8 and S9). Some slight disparity can be observed near our study locations: core PS118_63-1 for spring/summer sea-ice cover at PI (Fig. S4.3c), core PS67/219-1 for both winter sea-ice cover at PI (Fig. S5.3c) and for summer SST at 21 ka BP (Fig. S8.1c). However, the study sites remain spatially distinct from regions where the model-to-model agreement falls outside the 2σ threshold criterion. The significantly large model-to-model disparity illustrated in the sea-ice cover and SST plots for 21 ka BP can be linked to a denser and more extensive seasonal sea-ice cover simulated by COSMOS compared to the PMIP3 ensemble (Fig. 5.4 in main paper, Fig. S4.1 and S5.1). This expansiveness of sea ice simulated by COSMOS is consistently observed across simulations for the PI and 6 ka BP time slices. We note that Lunt et al. (2013) have demonstrated that COSMOS exhibits a milder warm bias in the Southern Ocean compared to several other PMIP3-grade models. This suggests that the larger sea-ice cover in COSMOS, relative to PMIP3, may indeed reflect a strength of the COSMOS simulation rather than a weakness.

While a comparison of model biases of PMIP4/CMIP6 and of COSMOS with respect to observations has not been explicitly made, CMIP6 models, on which PMIP4 is built, tend to show a warm bias in the Southern Ocean (Luo et al., 2023). Our comparison of COSMOS and PMIP4 sea-ice cover and SST simulation ensembles reveals a model-to-model disagreement that surpasses the discord with PMIP3 (Fig. S6c and S7c, S10c and S11c). Just as for PMIP3, COSMOS generally predicts a more expansive and denser sea-ice cover compared to PMIP4. Most significant differences between COSMOS and PMIP4 are found between 50-60ºS, and north of the sea ice border, with some variations observed along coastal regions. Additionally, higher levels of model-to-model discordance are observed at our study sites for PMIP4 than for PMIP3. Nevertheless, some level of agreement can still be observed for specific study locations. For instance, there is agreement in core site PS118_63-1 for winter sea-ice cover and winter SST (Fig. S7c and S11c), as well as at core site PS67/219-1 for winter sea-ice cover and winter SST at 21 ka BP (S7.3c and S11.3c). In several cases of model-discord at

core sites, the latter are in spatial proximity to regions where COSMOS and PMIP4 agree well with each other. We have shown that this COSMOS-to-PMIP4 contradictory outcome does not necessarily indicate a deficiency in the COSMOS model. Beyond different stages of model development, comparability of PMIP4 modeling protocols and boundary conditions to the PMIP3 framework, in which COSMOS has been employed for this study, is rather limited.

Despite different time slices being referenced for the Last Interglacial by COSMOS and PMIP4 ensemble, we still undertake a model-to-model comparison of PMIP4's 127 ka BP simulation against those of COSMOS's 128 and 125 ka BP simulations. The PMIP4 127 ka BP sea-ice cover shows better agreement with the 125 ka BP time slice of COSMOS. While larger disagreement is observed for the sea-ice cover simulated by COSMOS for 128 ka BP and for SST simulated by COSMOS at both 128 and 125 ka BP. COSMOS simulations for 125 and 128 ka BP are comparable to the PMIP4 127 ka BP time slice only to a very limited extent, owing to different forcings, boundary conditions, and modeling methodologies. Consequently, analysis of discrepancy between COSMOS and PMIP4 for the Last Interglacial should be viewed as an attempt to align our findings with the lig127k simulations available to the community, but not as an endorsement of any conclusion regarding COSMOS's skill in simulating the Last Interglacial climate.

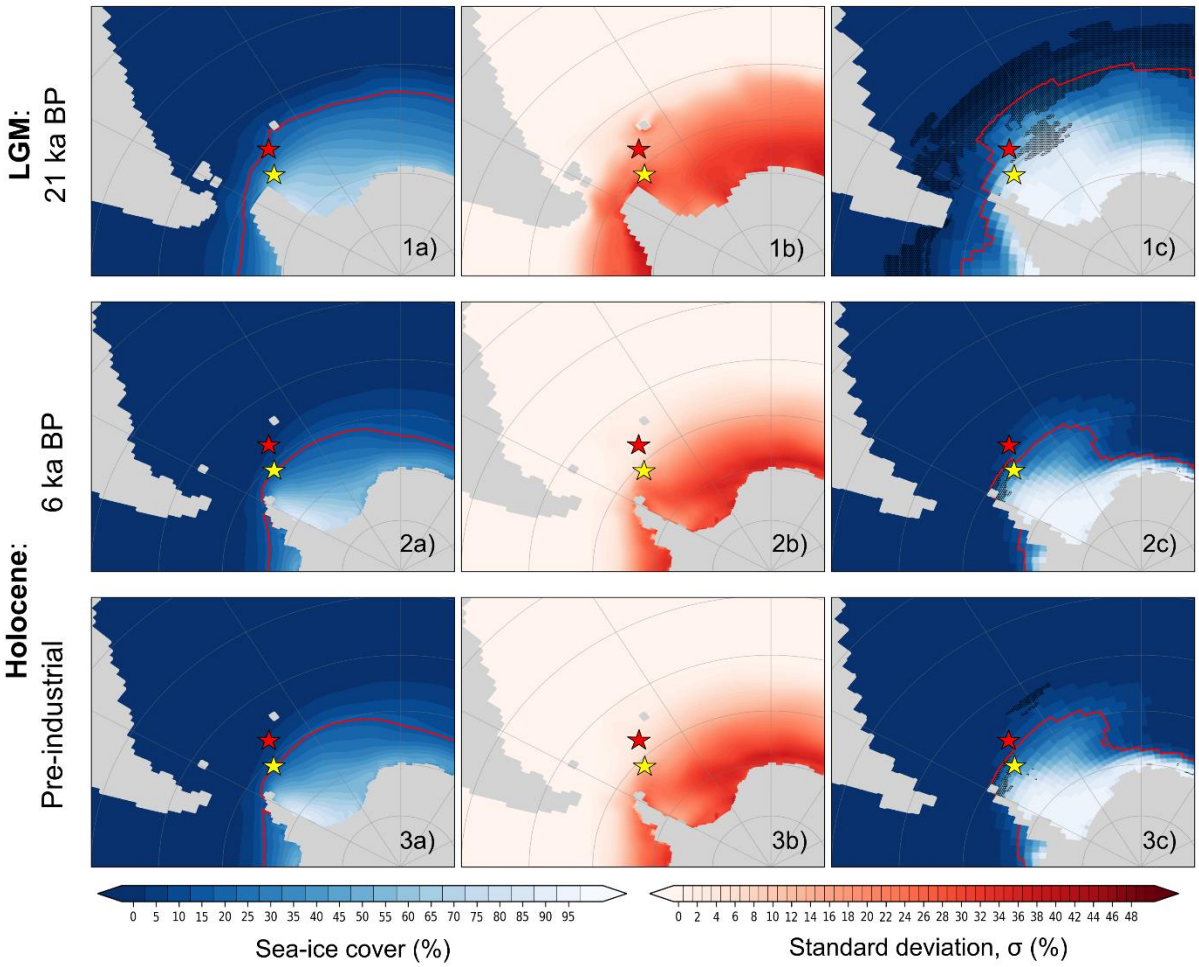

Figure S4. The spring/summer (NDJFMA) sea-ice cover data simulated by PMIP3 models for three distinct time slices: 1) 21 ka BP, 2) 6 ka BP and 3) Pre-industrial. The visuals include a) the PMIP3 ensemble mean, b) standard deviation, σ, and c) agreement (within 2σ threshold) of the COSMOS and PMIP3 simulation results. Results that deviate from the PMIP3 ensemble by more than 2σ are highlighted by stippling. The red line in panels a and c depicts the sea-ice extent – defined by the 15% isoline for sea ice coverage. Locations of marine sediment cores are indicated with stars: PS118_63-1 (yellow) and PS67/219-1 (red).

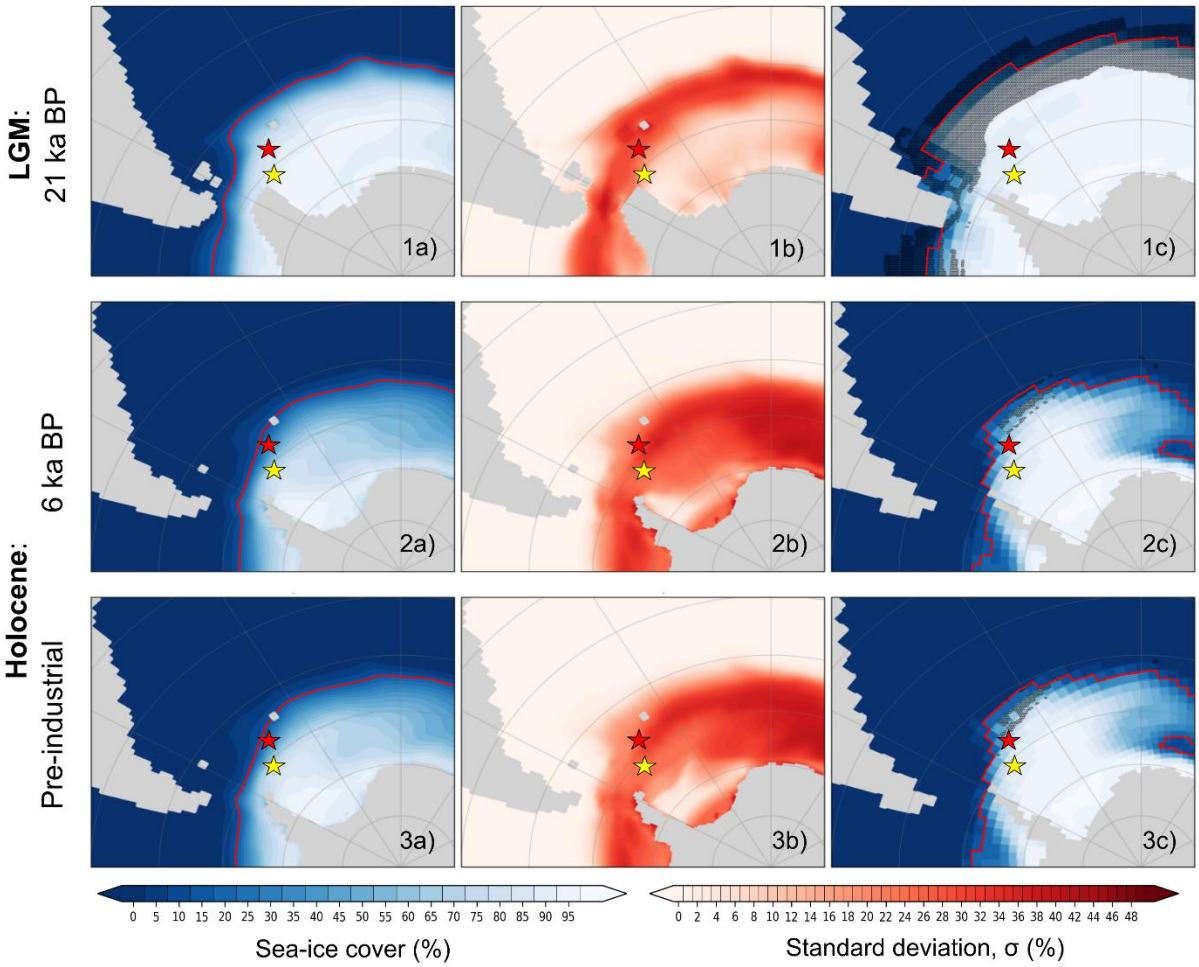

Figure S5. The winter (ASO) sea-ice cover data simulated by PMIP3 models for three distinct time slices: 1) 21 ka BP, 2) 6 ka BP and 3) Pre-industrial. The visuals include a) the PMIP3 ensemble mean, b) standard deviation, σ, and c) agreement (within 2σ threshold) of the COSMOS and PMIP3 simulation results. Results that deviate from the PMIP3 ensemble by more than 2σ are highlighted by stippling. The red line in panels a and c depicts the sea-ice extent – defined by the 15% isoline for sea ice coverage. Locations of marine sediment cores are indicated with stars: PS118_63-1 (yellow) and PS67/219-1 (red).

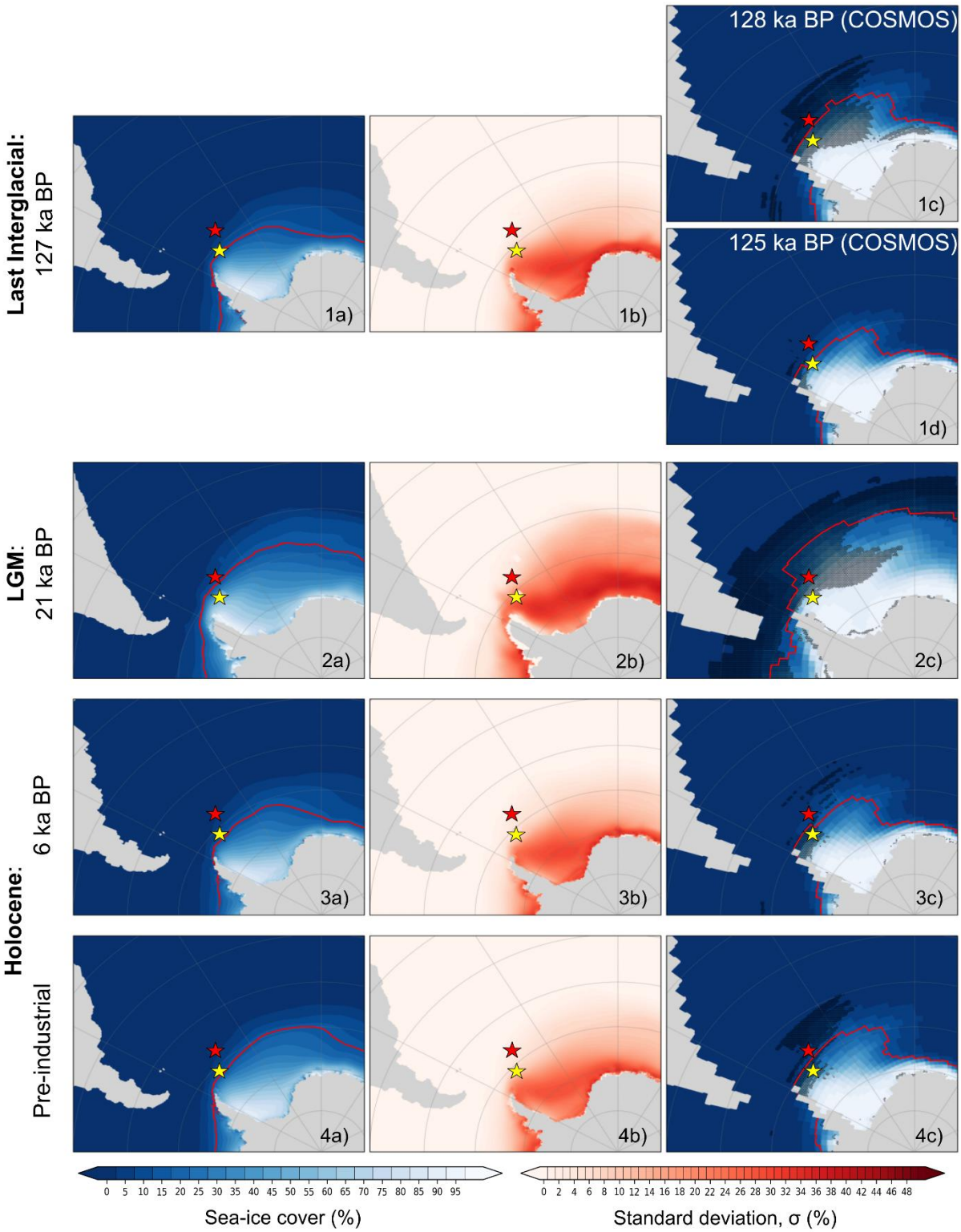

Figure S6. The spring/summer (NDJFMA) sea-ice cover simulation from PMIP4 models for various time slices, mainly 1) 127 ka BP, 2) 21 ka BP, 3) 6 ka BP and 4) Pre-industrial. The visuals include a) the PMIP4 ensemble mean, b) standard deviation, σ, and c) agreement (within 2σ threshold) of the COSMOS and PMIP3 simulation results. Results that deviate from the PMIP3 ensemble by more than 2σ are highlighted by stippling. Red line in panels a and c indicates the sea-ice extent – defined by the 15% isoline for sea ice coverage. Locations of marine sediment cores are indicated with stars: PS118_63-1 (yellow) and PS67/219-1 (red).

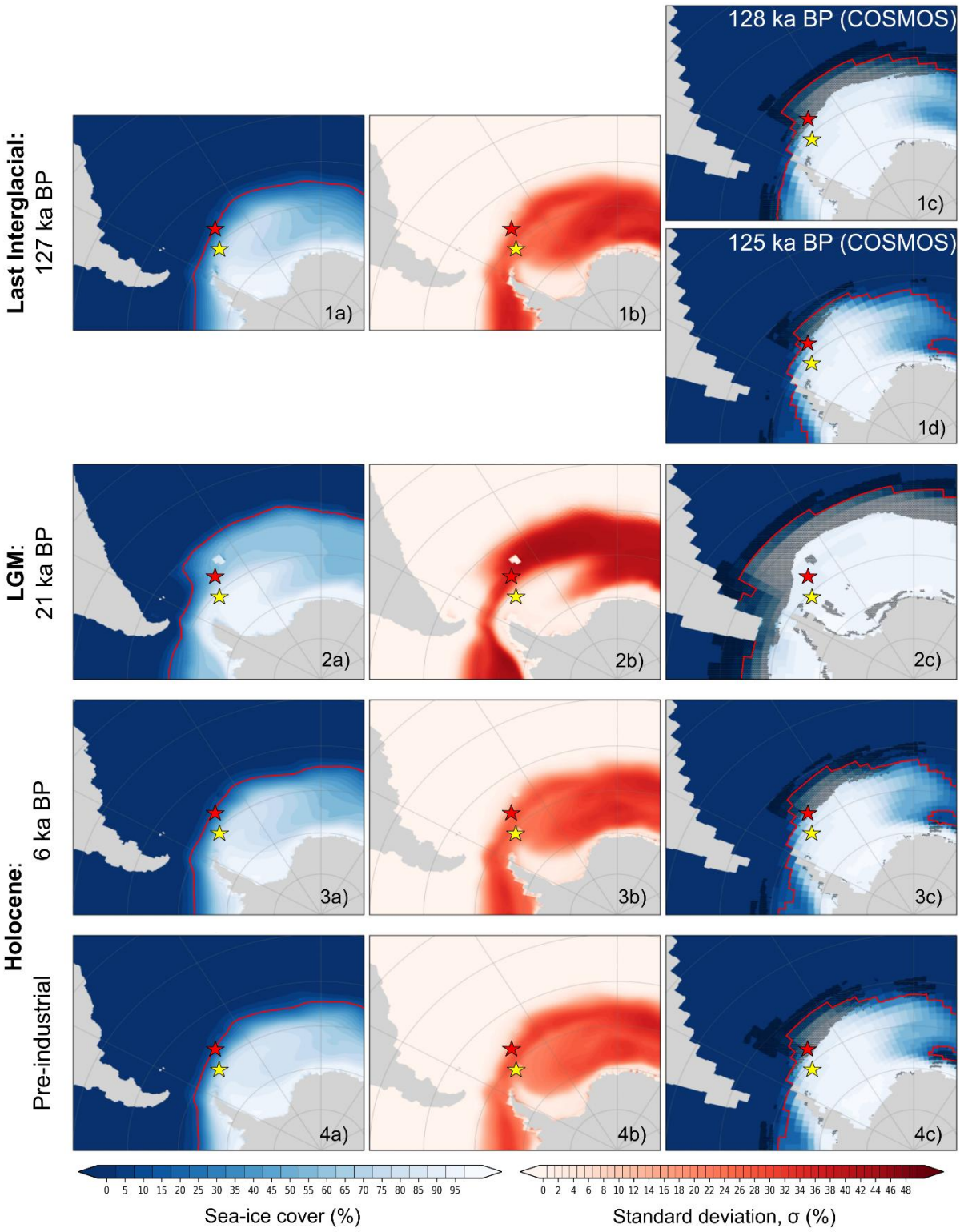

Figure S7. The winter (ASO) sea-ice cover simulation from PMIP4 models for various time slices, mainly 1) 127 ka BP, 2) 21 ka BP, 3) 6 ka BP and 4) Pre-industrial. The visuals include a) the PMIP4 ensemble mean, b) standard deviation, σ, and c) agreement (within 2σ threshold) of the COSMOS and PMIP3 simulation results. Results that deviate from the PMIP3 ensemble by more than 2σ are highlighted by stippling. Red line in panels a and c indicates the sea-ice extent – defined by the 15% isoline for sea ice coverage. Locations of marine sediment cores are indicated with stars: PS118_63-1 (yellow) and PS67/219-1 (red).

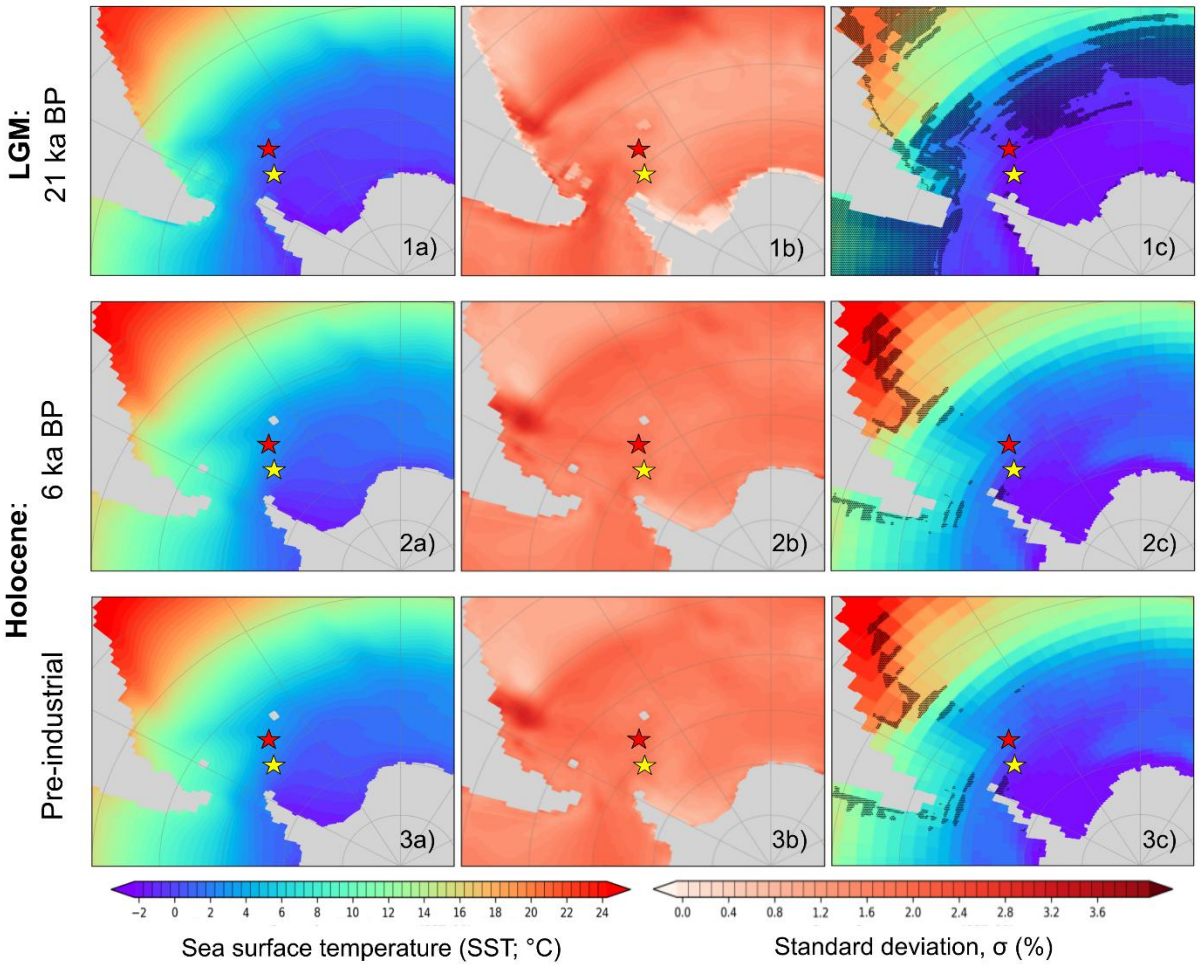

Figure S8. The summer (DJF) sea surface temperature simulated by PMIP3 models for three distinct time slices: 1) 21 ka BP, 2) 6 ka BP and 3) Pre-industrial. The visuals include a) the PMIP3 ensemble mean, b) standard deviation, σ, and c) agreement (within 2σ threshold) of the COSMOS and PMIP3 simulation results. Results that deviate from the PMIP3 ensemble by more than 2σ are highlighted by stippling. Locations of marine sediment cores are indicated with stars: PS118_63-1 (yellow) and PS67/219-1 (red).

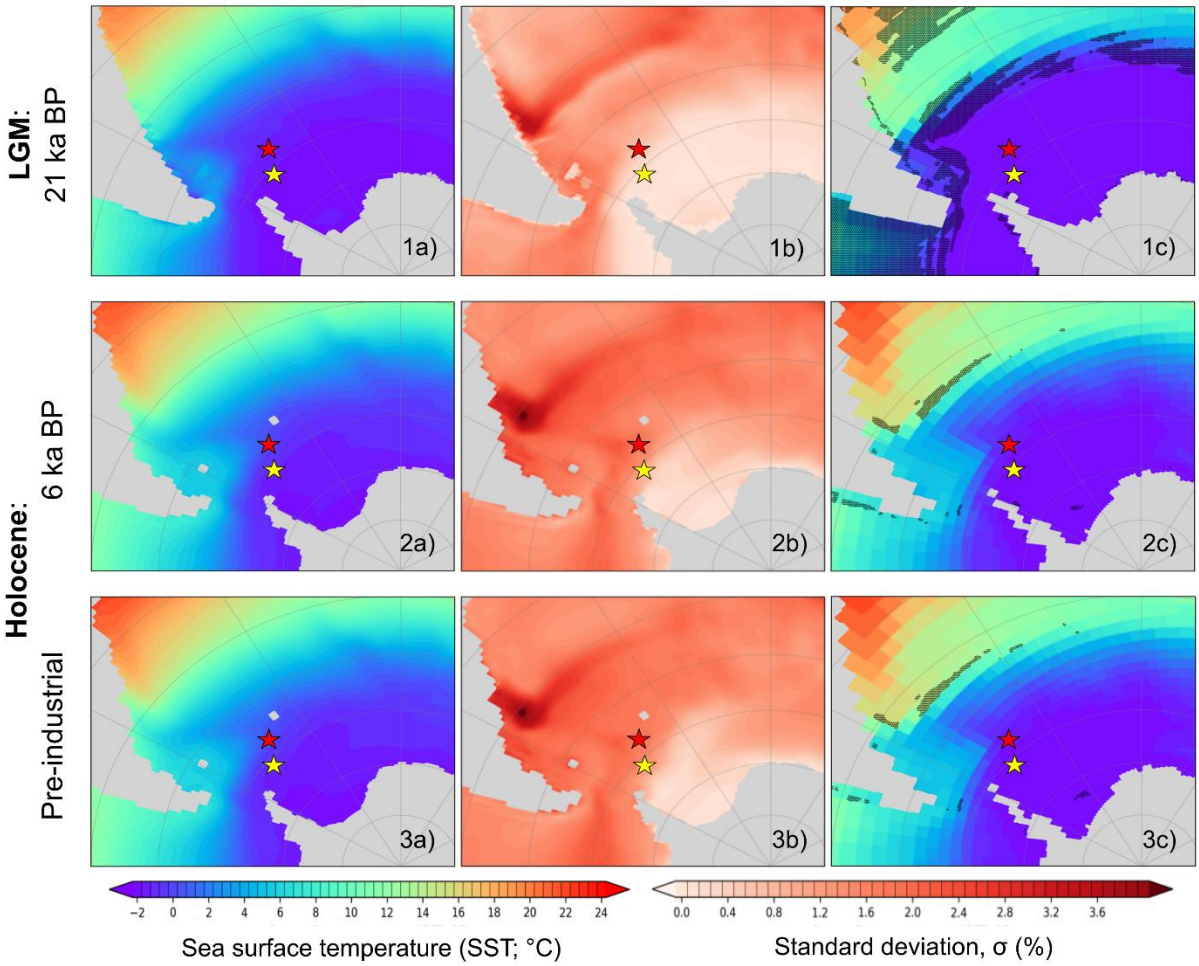

Figure S9. The winter (JJA) sea surface temperature simulated by PMIP3 models for three distinct time slices: 1) 21 ka BP, 2) 6 ka BP and 3) Pre-industrial. The visuals include a) the PMIP3 ensemble mean, b) standard deviation, σ, and c) agreement (within 2σ threshold) of the COSMOS and PMIP3 simulation results. Results that deviate from the PMIP3 ensemble by more than 2σ are highlighted by stippling. Locations of marine sediment cores are indicated with stars: PS118_63-1 (yellow) and PS67/219-1 (red).

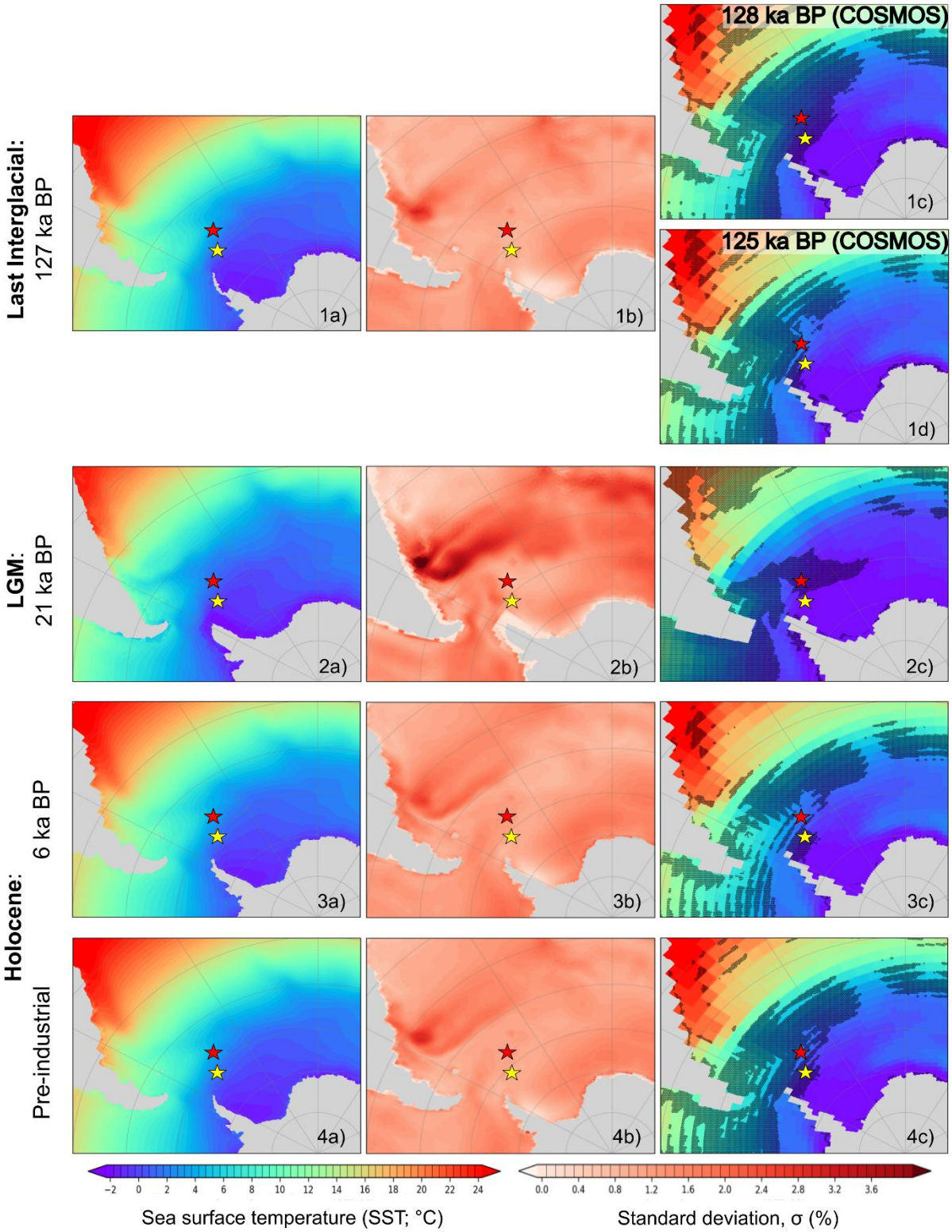

Figure S10. The summer (DJF) sea surface temperature simulation from PMIP4 models for various time slices, mainly 1) 127 ka BP, 2) 21 ka BP, 3) 6 ka BP and 4) Pre-industrial. The visuals include a) the PMIP4 ensemble mean, b) standard deviation, σ, and c) agreement (within 2σ threshold) of the COSMOS and PMIP3 simulation results. Results that deviate from the PMIP3 ensemble by more than 2σ are highlighted by stippling. Locations of marine sediment cores are indicated with stars: PS118_63-1 (yellow) and PS67/219-1 (red).

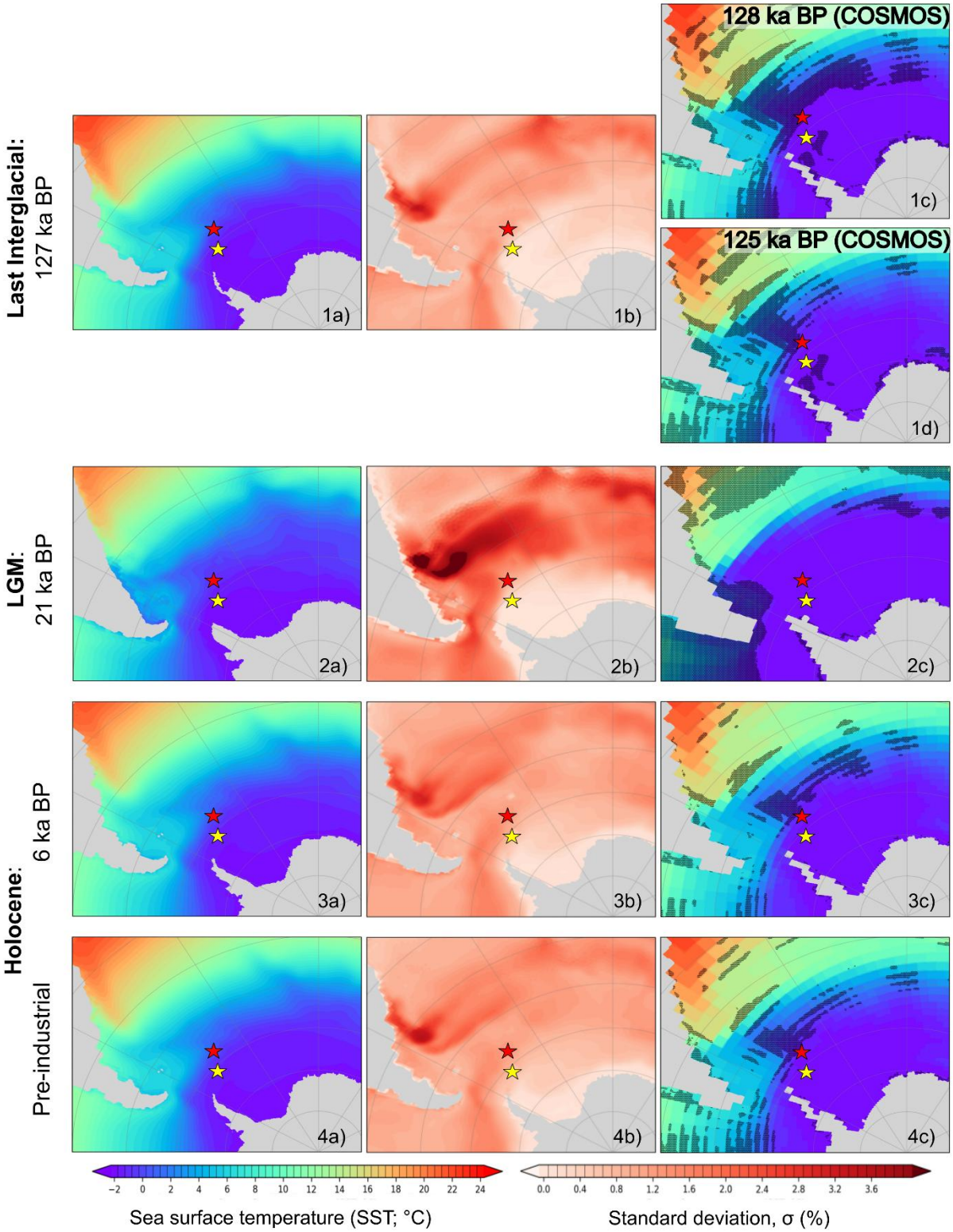

Figure S11. The winter (JJA) sea surface temperature simulation from PMIP4 models for various time slices, mainly 1) 127 ka BP, 2) 21 ka BP, 3) 6 ka BP and 4) Pre-industrial. The visuals include a) the PMIP4 ensemble mean, b) standard deviation, σ, and c) agreement (within 2σ threshold) of the COSMOS and PMIP3 simulation results. Results that deviate from the PMIP3 ensemble by more than 2σ are highlighted by stippling. Locations of marine sediment cores are indicated with stars: PS118_63-1 (yellow) and PS67/219-1 (red).

Table S3. Boundary conditions and model forcings for COSMOS simulations. We present: forcing values of eccentricity of the Earth's orbit (ecc), obliquity of the Earth's rotation axis (obld), longitude of the perihelion of the Earth's orbit (lonp); atmospheric concentrations of greenhouse gas species carbon dioxide (CO_2), methane, (CH_4), nitrous oxide (N_2O); where applicable, we provide references (ref) to employed paleogeography, orbital forcing, atmospheric greenhouse gas forcing, and to a previous study that provides additional details and description for each specific simulation.

Simulation	**Orbital forcing**				**Greenhouse gas forcing**				**Paleography**		**Previously published by**	
	ecc	**obld (°)**	**Lonp (°)**	**ref**	**CO_2 (ppm)**	**CH_4 (ppb)**	**N_2O (ppb)**	**ref**	**reconstruction**	**ref**	**ref**	**name in ref**
piControl	0.016724	23.4468	282.157	Berger (1978)	280	760	270	Crucifix et al. (2005)	—	—	Wei and Lohmann (2012)	CTL
mh6k	0.018682	24.1048	180.918	Berger (1978)	280	650	270	Crucifix et al. (2005) (as PMIP3 6ka)	—	—	Wei and Lohmann (2012)	H6K
lgm21k	0.018994	22.949	114.42	Braconnot and Kageyama (2015) and references therein	185	350	200	PMIP3 21ka Braconnot and Kageyama (2015) and references therein	PMIP3 21ka	Braconnot and Kageyama (2015) and references therein	Zhang et al. (2013)	LGMW
lig125k	0.040013	23.798	127.14	PMIP3 125ka Lunt et al. (2013)	275.938	640.417	263.084	PMIP3 125ka Lunt et al. (2013)	as *piControl*	—	this study	—
lig128k	0.039017	24.131	79.65	PMIP3 128ka Lunt et al. (2013)	275	709	512	128ka Lunt et al. (2013)	as *piControl*	—	this study	—
pgm140k	0.032796	23.4138	253.244	Berger et al. (1978)	185	350	200	as *lgm21k*	as *lgm21k*	as *lgm21k*	this study	—

Table S4. Summary of the specific models (and their references; see remarks), variables, and data types utilize in the COSMOS to PMIP comparison in this study. Unless otherwise noted, we employ realization r1i1p1 for CMIP5/PMIP3 and r1i1p1f1 for CMIP6/PMIP4.

Simulations	Variables	Climate models	Type of data
CMIP5/PMIP3 ensemble models			
piControl	sic & tos	BCC-CSM1-1[1], CCSM4[2], CNRM-CM5[3], CSIRO-Mk3-6-0[4], CSIRO-Mk3L-1-2[5], EC-EARTH-2-2[6], GISS-E2-R[7], HadGEM2-CC[8], HadGEM2-ES[8], IPSL-CM5A-LR[9], MIROC-ESM[10], MPI-ESM-P[11], MRI-CGCM3[12]	monthly mean
	sic only	FGOALS-s2[13]	
	tos only	KCM1-2-2[14]	
mid-Holocene	sic & tos	BCC-CSM1-1[1], CCSM4[2], CNRM-CM5[3], CSIRO-Mk3-6-0[4], CSIRO-Mk3L-1-2[5], EC-EARTH-2-2[6], FGOALS-s2[13], GISS-E2-R[7], HadGEM2-CC[8], HadGEM2-ES[8], IPSL-CM5A-LR[9], MPI-ESM-P[11,15]	monthly mean
	sic only	MIROC-ESM[10], MRI-CGCM3[12]	climatological monthly mean
	tos only	KCM1-2-2[14]	monthly mean
lgm	sic & tos	CNRM-CM5[3], IPSL-CM5A-LR[9]	monthly mean
		CCSM4[2], GISS-E2-R[16], MIROC-ESM[10], MPI-ESM-P[11], MRI-CGCM3[12]	climatological monthly mean
CMIP6/PMIP4 ensemble models			
piControl	siconc & tos	ACCESS-ESM1-5[17], AWI-ESM-1-1-LR[18], CESM2[19], CESM2-FV2[20], CESM2-WACCM-FV2[21], CNRM-CM6-1[22], EC-Earth3-LR[23], FGOALS-g3[24], HadGEM3-GC31-LL[25], INM-CM4-8[26], IPSL-CM6A-LR[27], MIROC-ES2L[28], MPI-ESM1-2-LR[29], MRI-ESM2-0[30], NESM3[31], NorESM1-F[32], NorESM2-LM[33]	monthly mean
	tos only	FGOALS-f3-L[34] and GISS-E2-1-G[35]	
mid-Holocene	siconc & tos	ACCESS-ESM1-5[36], CESM2[37], EC-Earth3-LR[38], FGOALS-f3-L[39], FGOALS-g3[40], INM-CM4-8[41], IPSL-CM6A-LR[42], MIROC-ES2L[43], MPI-ESM1-2-LR[44], MRI-ESM2-0[45], NESM3[46], NorESM1-F[47], NorESM2-LM[48]	monthly mean
	tos only	GISS-E2-1-G[49] and HadGEM3-GC31-LL[50]	
lgm	siconc & tos	AWI-ESM-1-1-LR[51], MIROC-ES2L[52], MPI-ESM1-2-LR[53]	monthly mean
	tos only	INM-CM4-8[54]	
lig127k	siconc & tos	ACCESS-ESM1-5[55], AWI-ESM-1-1-LR[56], CESM2[57], CNRM-CM6-1[58], EC-Earth3-LR[59], FGOALS-g3[60], IPSL-CM6A-LR[61], NESM3[62], NorESM1-F[63], NorESM2-LM[64]	monthly mean
	siconc only	FGOALS-f3-L[65], MIROC-ES2L[66]	
	tos only	HadGEM3-GC31-LL[67]	

Remarks:
[1]Beijing Climate Center (BCC), China Meteorological Administration, China
[2]National Center for Atmospheric Research (NCAR), United States of America
[3]Centre National de Recherches Météorologiques/Centre Européen de Recherche et Formation Avancées en Calcul Scientifique (CNRM/CERFACS), France
[4]Commonwealth Scientific and Industrial Research Organization (CSIRO), Queensland Climate Change Centre of Excellence (QCCCE), Australia
[5]University of New South Wales (UNSW), Australia
[6]EC-EARTH consortium
[7]NASA Goddard Institute for Space Studies, United States of America
[8]Met Office Hadley Centre, United Kingdom
[9]Institut Pierre-Simon Laplace, France

[10]Japan Agency for Marine-Earth Science and Technology (JAMSTEC), Atmosphere and Ocean Research Institute (AORI, The University of Tokyo), National Institute for Environmental Studies (NIES), Japan
[11]Max Planck Institute for Meteorology (MPI-M), Germany
[12]Meteorological Research Institute (MRI), Japan
[13]Institute of Atmospheric Physics (IAP), Chinese Academy of Sciences (CAS), China
[14]GEOMAR Helmholtz Center for Ocean Research (GEOMAR), Christian-Albrechts University of Kiel (CAU), Germany
[15]For the CMIP5/PMIP3 *midHolocene* simulation, MPI-ESM-P provides only the variable tos as monthly mean model output, while the variable sic has been derived from monthly climatological mean available through ESGF.
[16]NASA Goddard Institute for Space Studies, United States of America; r1i1p150 used
[17]Ziehn et al. (2019)
[18]Danek et al. (2020)
[19]Danabasoglu et al. (2019)
[20]Danabasoglu (2019a)
[21]Danabasoglu (2019b)
[22]Voldoire (2018)
[23]EC-Earth Consortium (2019)
[24]Li (2019)
[25]Ridley et al. (2018)
[26]Volodin et al. (2019a)
[27]Boucher et al. (2018a)
[28]Hajima et al. (2019); r1i1p1f2 used
[29]Wieners et al. (2019)
[30]Yukimoto et al. (2019a)
[31]Cao and Wang (2019)
[32]Guo et al. (2019a)
[33]Seland et al. (2019)
[34]Yu (2019)
[35]Nasa Goddard Institute for Space Studies (2018)
[36]Brown et al. (2021)
[37]Danabasoglu (2019c)
[38]EC-Earth Consortium (2020a)
[39]Zheng and He (2019a)
[40]Zheng and Dong (2019a)
[41]Volodin et al. (2019b)
[42]Boucher et al. (2018b); r1i2p1f1 used
[43]Ohgaito et al. (2019a); r1i1p1f2 used
[44]Jungclaus et al. (2019a)
[45]Yukimoto et al. (2019b)
[46]Cao (2019a)
[47]Guo et al. (2019b)
[48]Zhang et al. (2019a)
[49]Nasa Goddard Institute for Space Studies (2019)
[50]Williams et al. (2021a)
[51]Shi et al. (2020a)
[52]Ohgaito et al. (2019b); r1i1p1f2 used
[53]Jungclaus et al. (2019b)
[54]Volodin et al. (2019c)
[55]Yeung et al. (2019)
[56]Shi et al. (2020b)
[57]Danabasoglu (2019d)
[58]Voldoire (2020); r1i1p1f2 used
[59]Earth Consortium (2020b)
[60]Zheng and Dong (2019b)
[61]Boucher et al. (2018c)
[62]Cao (2019b)
[63]Guo et al. (2019c)
[64]Zhang et al. (2019b)
[65]Zheng and He (2019b)
[66]O'ishi et al. (2019); r1i1p1f2 used
[67]Williams et al. (2021b)

Table S5. This table summarizes the simulated data from (a) CMIP5 and (b) CMIP6 frameworks available on the ESGF. Simulations are grouped, in columns, by the studied time slices used in this work, with the CMIP and PMIP simulation names given in brackets where such simulations are available. This table illustrates sparseness of coverage relevant to our study by ensembles from the community. Models with at least one relevant dataset are highlighted in green. In our analysis we only considered models that provide data for at least one additional time slice beyond PI. Note that relevant simulations and variables may not necessarily overlap, and that lengths of available time series differ between models. In cases where only one specific variable (i.e., sea surface temperature or sea-ice cover only) is available, this is indicated in the table (e.g., "sic only" for availability of variable sic and unavailability of variable tos). Data from models that were unavailable due to prolonged server downtime are marked in orange. Please refer to the remarks for further information on data availability. Data accessed from ESGF (https://esgf-data.dkrz.de/search/cmip6-dkrz/; https://esgf-data.dkrz.de/search/esgf-dkrz/; accessed 3rd of April, 2024).

a) Simulations related to CMIP5 and PMIP3

	PI (*piControl*)	6 ka BP (*midHolocene*)	21 ka BP (*lgm*)	125 ka BP	127 ka BP	128 ka BP	140 ka BP
ACCESS1.0							
ACCESS1.3							
BCC-CSM1.1							
CCSM4							
CMCC-CESM							
CMCC-CM							
CMCC-CMS							
CNRM-CM5							
CNRM-CM5-2							
CSIRO-Mk3.6.0							
CSIRO-Mk3L-1-2							
CanESM2							
EC-EARTH							
EC-EARTH-2-2							
FGOALS-g2							
FGOALS-s2	sic only[1]						
GISS-E2-H							
GISS-E2-H-CC							
GISS-E2-R							
GISS-E2-R-CC							
HadCM3							
HadGEM2-AO							
HadGEM2-CC							
HadGEM2-ES							
INM-CM4							
IPSL-CM5A-LR							
IPSL-CM5A-MR							
IPSL-CM5B-LR							
KCM1-2-2	tos only[2]	tos only[3]					
MIROC-ESM							
MIROC-ESM-CHEM							
MIROC4h							
MIROC5							
MPI-ESM-LR							
MPI-ESM-MR							
MPI-ESM-P							
MRI-CGCM3							
NorESM1-M							
NorESM1-ME							
bccr bcm2 0							
cccma cgcm3 1							
cccma cgcm3 1 t63							

a) Simulations related to CMIP5 and PMIP3 (cont.)							
	PI (*piControl*)	6 ka BP (*midHolocene*)	21 ka BP (*lgm*)	125 ka BP	127 ka BP (*lig127k*)	128 ka BP	140 ka BP
cnrm cm3							
csiro mk3 0							
csiro mk3 5							
gfdl cm2 0							
gfdl cm2 1							
giss aom							
giss model e h							
giss model e r							
iap fgoals1 0 g							
ingv echam4							
inmcm3 0							
ipsl cm4							
miroc3 2 hires							
miroc3 2 medres							
miub echo g							
mri cgcm2 3 2a							
ncar ccsm3 0							
ncar pcm1							
ukmo hadcm3							
ukmo hadgem1							

b) Simulations related to CMIP6 and PMIP4

	PI (*piControl*)	6 ka BP (*midHolocene*)	21 ka BP (*lgm*)	125 ka BP	127 ka BP (*lig127k*)	128 ka BP	140 ka BP
ACCESS-CM2							
ACCESS-ESM1-5							
AWI-CM-1-1-MR							
AWI-ESM-1-1-LR							
BCC-CSM2-MR							
BCC-ESM1							
CAMS-CSM1-0							
CAS-ESM2-0							
CESM2							
CESM2-FV2			offline[4]				
CESM2-WACCM							
CESM2-WACCM-FV2			offline[5]				
CIESM							
CMCC-CM2-SR5							
CMCC-ESM2							
CNRM-CM6-1							
CNRM-CM6-1-HR							
CNRM-ESM2-1							
CanESM5							
CanESM5-1							
CanESM5-CanOE							
E3SM-1-0							
E3SM-1-1							
E3SM-1-1-ECA							
E3SM-2-0							
E3SM-2-0-NARRM							
EC-Earth3							
EC-Earth3-AerChem							
EC-Earth3-CC							
EC-Earth3-LR							
EC-Earth3-Veg							
EC-Earth3-Veg-LR							

b) Simulations related to CMIP6 and PMIP4 (cont.)							
	PI (*piControl*)	6 ka BP (*midHolocene*)	21 ka BP (*lgm*)	125 ka BP	127 ka BP (*lig127k*)	128 ka BP	140 ka BP
FGOALS-f3-L	**tos only[6]**				**siconc only[7]**		
FGOALS-g3							
FIO-ESM-2-0							
GFDL-ESM4							
GISS-E2-1-G	**tos only[8]**	**tos only[9]**			**offline[10]**		
GISS-E2-1-H							
GISS-E2-2-G							
GISS-E2-2-H							
HadGEM3-GC31-LL		**tos only[11]**			**tos only[12]**		
HadGEM3-GC31-MM							
ICON-ESM-LR							
IITM-ESM							
INM-CM4-8			**tos only[13]**				
INM-CM5-0							
IPSL-CM5A2-INCA							
IPSL-CM6A-LR							
IPSL-CM6A-MR1							
KIOST-ESM							
MCM-UA-1-0							
MIROC-ES2H							
MIROC-ES2L					**siconc only[14]**		
MIROC6							
MPI-ESM-1-2-HAM							
MPI-ESM1-2-HR							
MPI-ESM1-2-LR							
MRI-ESM2-0							
NESM3							
NorCPM1							
NorESM1-F							
NorESM2-LM							
NorESM2-MM							
SAM0-UNICON							
TaiESM1							
UKESM1-0-LL							
UKESM1-1-LL							

Remarks:

[1] For simulation *piControl*, model FGOALS-s2 provides both variables tos and sic; yet, data for variable tos has not been accessible via ESGF due to unavailability of data node esg.lasg.ac.cn that, at the time of data access, provides the only copy of that data.

[2] For simulation *piControl*, model KCM1-2-2 only provides via ESGF data for variable tos, but not for variable sic.

[3] For simulation *midHolocene*, model KCM1-2-2 only provides via ESGF data for variable tos, but not for variable sic.

[4] For simulation *lgm*, model CESM-FV2 provides both variables tos and sic; yet, for both variables data has not been accessible via ESGF due to unavailability of data nodes esgf-data.ucar.edu and esgf-data1.llnl.gov that, at the time of data access, provide the only copy of that data.

[5] For simulation *lgm*, model CESM-WACCM-FV2 provides both variables tos and sic; yet, for both variables data has not been accessible via ESGF due to unavailability of data nodes esgf-data.ucar.edu and esgf-data1.llnl.gov that, at the time of data access, provide the only copy of that data.

[6] For simulation *piControl*, model FGOALS-f3-L only provides via ESGF data for variable tos, but not for variable siconc.

[7] For simulation *lig127k*, model FGOALS-f3-L provides both variables tos and siconc; yet, data for variable tos has not been accessible via ESGF due to unavailability of data nodes esg.lasg.ac.cn and esgf-data1.llnl.gov that, at the time of data access, provide the only copy of that data.

[8] For simulation *piControl*, model GISS-E2-1-G only provides via ESGF data for variable tos, but not for variable siconc.

[9] For simulation *midHolocene*, model GISS-E2-1-G only provides via ESGF data for variable tos, but not for variable siconc.

[10] For simulation *lig127k*, model GISS-E2-1-G provides both variables tos and siconc; yet, for both variables data has not been accessible via ESGF due to unavailability of data nodes esgf-data1.llnl.gov, dpesgf03.nccs.nasa.gov, and esgf-data04.diasjp.net that, at the time of data access, provide the only copy of that data.

[11] For simulation *midHolocene*, model HadGEM3-GC31-LL only provides via ESGF data for variable tos, but not for variable siconc.

[12] For simulation *lig127k*, model HadGEM3-GC31-LL only provides via ESGF data for variable tos, but not for variable siconc.

[13] For simulation *lgm*, model INM-CM4-8 only provides via ESGF data for variable tos, but not for variable siconc.

[14] For simulation *lig127k,* model MIROC-ES2L provides both variables tos and siconc; yet, data for variable tos has not been accessible via ESGF due to unavailability of data nodes esgf-data02.diasjp.net and esgf-data1.llnl.gov that, at the time of data access, provide the only copy of that data.

S4: Productivity signals

The concentration of total isoprenoid glycerol dialkyl glycerol tetraether lipids (isoGDGTs) and hydroxylated (OH)-GDGTs, synthetized from marine archaea (Schouten et al., 2013), varies between 1.36-358.32 µg/g OC and 0.01-105.71 µg/g OC, respectively (Fig. S4d). The concentration of total branched GDGTs (brGDGTs), mainly derived from terrestrial bacteria or eukaryotes in soils and peats (Hopmans et al., 2004), ranges between 0.11 and 7.34 µg/g OC (Fig. S4e). Lastly, the concentration of phytosterols fluctuates between 0-54.28 µg/g OC (Brassicasterol) and 0-8.51 µg/g OC (Dinosterol; Fig. S4f). The opal ($bSiO_2$) and brassicasterol profiles (Fig. S4b and f), often used as diatom productivity indicators, exhibit contrasting trends, especially between 140-110 ka BP. This discrepancy likely arises from the limited presence of brassicasterol-producing diatoms in the area, further affected by preferential growth conditions and preservation effects. As a result, the brassicasterol-producing diatoms signal is consistently attenuated within the overall opal signal (Badejo et al., 2017; Cavagna et al., 2013).

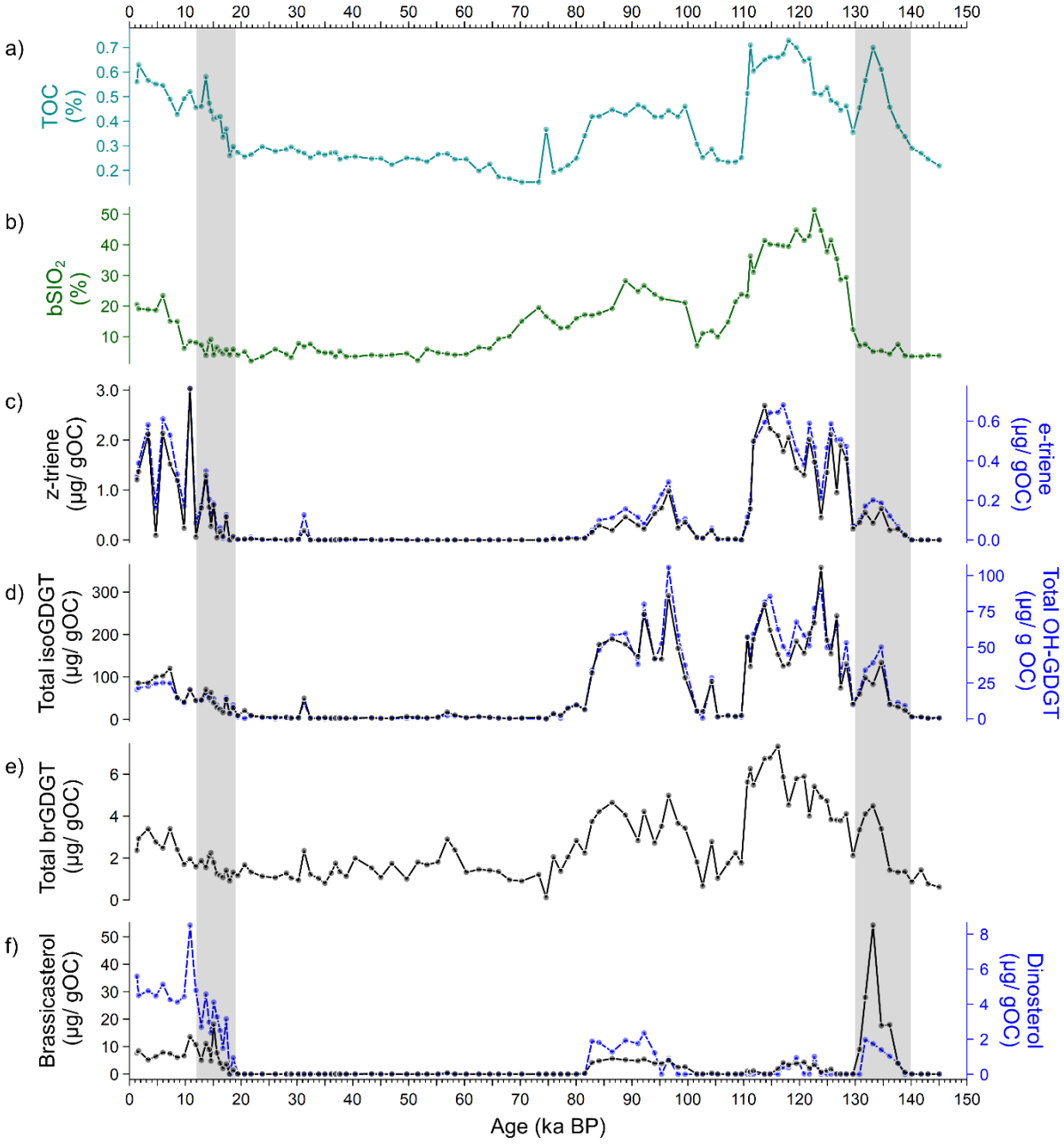

Figure S12. Plots of organic matter signals from core PS118_63-1: a) TOC, b) biogenic opal, c) HBI-based phytoplankton, d) total isoprenoid-GDGT and total hydroxylated-GDGT, e) total branched-GDGT and f) phytosterols. Shaded intervals indicate Termination 1 and Termination II, respectively.

S5: TEX_{86}^{L}-derived subsurface ocean temperature and GDGT-related indices

The TEX_{86}^{L}-derived subsurface ocean temperature (OT; Fig. S5a) shows a temperature range between -2.6 and 1.0°C at the core site. However, a review of the GDGT-related indices (Fig. S5b-e) provide strong evidence of factors that result in biasness in our TEX_{86}^{L}-based temperature reconstruction, especially during MIS 2-4, 5d and 6. For example, an isoGDGT-[2]/[3] ratio greater than five indicates contribution from deep-dwelling archaea (>1000 m water depth), which are regulated by processes different than that of their surface water counterparts (Kim et al., 2015; Taylor et al., 2013). A higher abundance of isoGDGT-0 relative to crenarchaeol (%isoGDGT-0 value > 67%) also suggests a methanogenic source for the isoGDGT-0 (Inglis et al., 2015). Lastly, values of ΔRI and BIT indices that are higher than 0.3, imply inputs from potential nonthermal influences and/or terrestrial origin, respectively (Fietz et al., 2016; Park, 2019; Weijers et al., 2006; Zhang et al., 2016).

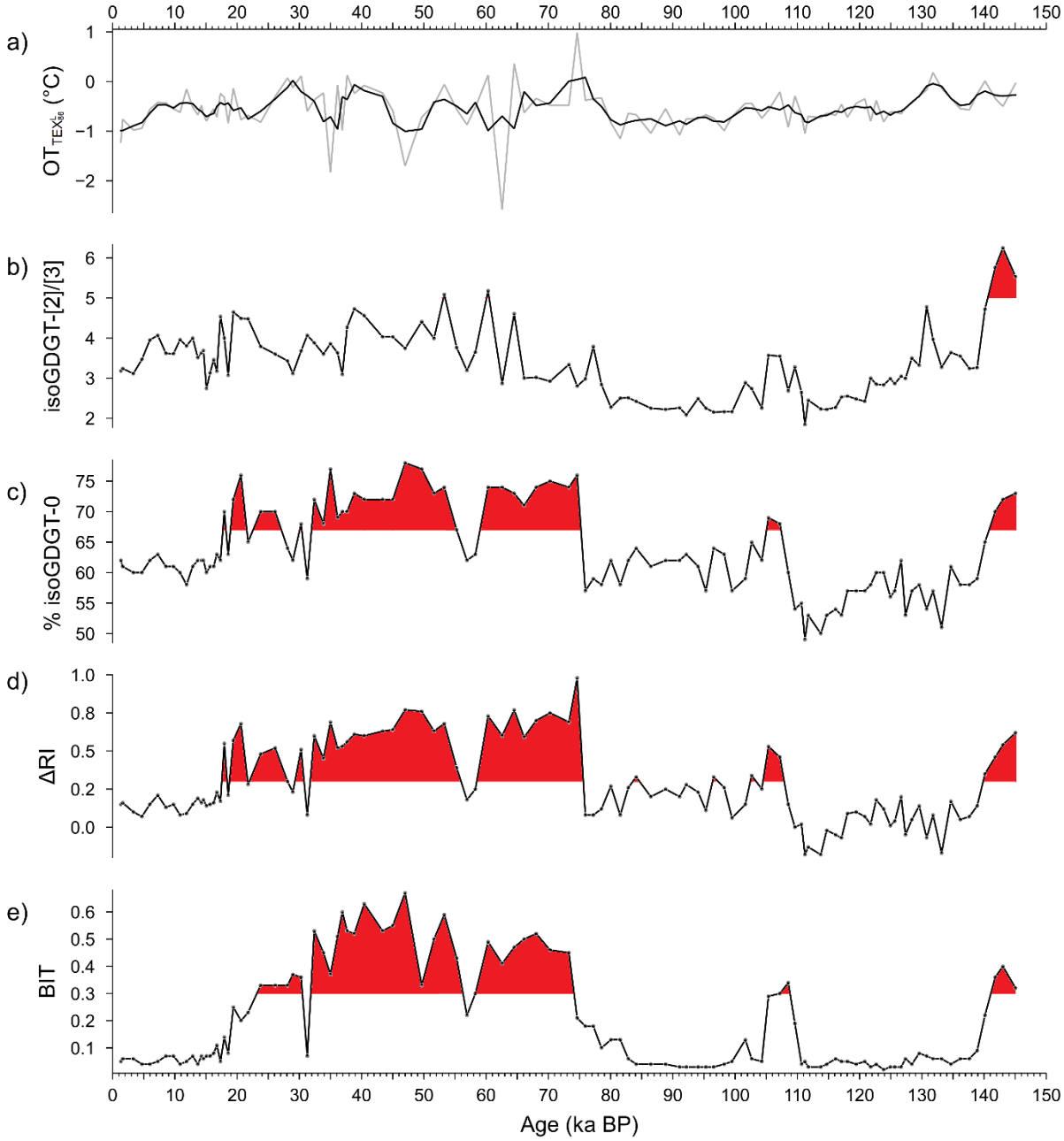

Figure S13. Records of a) TEX_{86}^{L}-derived ocean temperature and respective isoGDGT-related indices: b) isoGDGT [2]/[3], c) %isoGDGT-0, d) delta ring index and e) BIT for core PS118_63-1. Intervals with strong non-thermal influences are highlighted in red on the various index curves: isoGDGT [2]/[3] > 5.0, %isoGDGT-0 > 67%, ΔRI and BIT > 0.3.

References

Appleby, P. G. and Oldfield, F.: The calculation of lead-210 dates assuming a constant rate of supply of unsupported 210Pb to the sediment, Catena, 5, 1-8, https://doi.org/10.1016/S0341-8162(78)80002-2, 1978.

Badejo, A. O., Seo, I., Kim, W., Hyeong, K., and Ju, S.-J.: Effect of eolian Fe-supply change on the phytoplankton productivity and community in central equatorial Pacific Ocean during the Pleistocene: A lipid biomarker approach, Organic Geochemistry, 112, 170-176, https://doi.org/10.1016/j.orggeochem.2017.07.010, 2017.

Bakker, P., Masson-Delmotte, V., Martrat, B., Charbit, S., Renssen, H., Gröger, M., Krebs-Kanzow, U., Lohmann, G., Lunt, D. J., Pfeiffer, M., Phipps, S. J., Prange, M., Ritz, S. P., Schulz, M., Stenni, B., Stone, E. J., and Varma, V.: Temperature trends during the Present and Last Interglacial periods – a multi-model-data comparison, Quaternary Science Reviews, 99, 224-243, https://doi.org/10.1016/j.quascirev.2014.06.031, 2014.

Berger, A.: Long-Term Variations of Daily Insolation and Quaternary Climatic Changes, Journal of Atmospheric Sciences, 35, 2362-2367, https://doi.org/10.1175/1520-0469(1978)035<2362:LTVODI>2.0.CO;2, 1978.

Bianchi, C. and Gersonde, R.: The Southern Ocean surface between Marine Isotope Stages 6 and 5d: Shape and timing of climate changes, Palaeogeography, Palaeoclimatology, Palaeoecology, 187, 151-177, https://doi.org/10.1016/S0031-0182(02)00516-3, 2002.

Blaauw, M. and Christen, J. A.: Flexible paleoclimate age-depth models using an autoregressive gamma process, Bayesian Analysis, 6, 457-474, 418, https://doi.org/10.1214/11-BA618, 2011.

Boucher, O., Denvil, S., Levavasseur, G., Cozic, A., Caubel, A., Foujols, M.-A., Meurdesoif, Y., Braconnot, P., Contoux, C., Kageyama, M., and Khodri, M.: IPSL IPSL-CM6A-LR model output prepared for CMIP6 PMIP midHolocene, Version 20180926, Earth System Grid Federation, https://doi.org/10.22033/ESGF/CMIP6.5229, 2018b.

Boucher, O., Denvil, S., Levavasseur, G., Cozic, A., Caubel, A., Foujols, M.-A., Meurdesoif, Y., Braconnot, P., Contoux, C., Kageyama, M., and Khodri, M.: IPSL IPSL-CM6A-LR model output prepared for CMIP6 PMIP lig127k, Version 20180926, Earth System Grid Federation, https://doi.org/10.22033/ESGF/CMIP6.5228, 2018c.

Boucher, O., Denvil, S., Levavasseur, G., Cozic, A., Caubel, A., Foujols, M.-A., Meurdesoif, Y., Cadule, P., Devilliers, M., Ghattas, J., Lebas, N., Lurton, T., Mellul, L., Musat, I., Mignot, J., and Cheruy, F.: IPSL IPSL-CM6A-LR model output prepared for CMIP6 CMIP piControl, Earth System Grid Federation, Version 20200326, Earth System Grid Federation, https://doi.org/10.22033/ESGF/CMIP6.5251, 2018a.

Braconnot, P. and Kageyama, M.: Shortwave forcing and feedbacks in Last Glacial Maximum and Mid-Holocene PMIP3 simulations, Philosophical Transactions of the Royal Society A: Mathematical, Physical and Engineering Sciences, 373, 20140424, https://doi.org/10.1098/rsta.2014.0424, 2015.

Braconnot, P., Harrison, S. P., Kageyama, M., Bartlein, P. J., Masson-Delmotte, V., Abe-Ouchi, A., Otto-Bliesner, B., and Zhao, Y.: Evaluation of climate models using palaeoclimatic data, Nature Climate Change, 2, 417-424, https://doi.org/10.1038/nclimate1456, 2012.

Brown, J., Yeung, N., Menviel, L., Meissner, K., Ziehn, T., Chamberlain, M., Mackallah, C., Druken, K., and Ridzwan, S. M.: CSIRO ACCESS-ESM1.5 model output prepared for CMIP6 PMIP midHolocene, Version 20210422, Earth System Grid Federation, https://doi.org/10.22033/ESGF/CMIP6.13704, 2021.

Burls, N. J., Bradshaw, C. D., De Boer, A. M., Herold, N., Huber, M., Pound, M., Donnadieu, Y., Farnsworth, A., Frigola, A., Gasson, E., von der Heydt, A. S., Hutchinson, D. K., Knorr, G., Lawrence, K. T., Lear, C. H., Li, X., Lohmann, G., Lunt, D. J., Marzocchi, A., Prange, M., Riihimaki, C. A., Sarr, A.-C., Siler, N., and Zhang, Z.: Simulating Miocene Warmth: Insights From an Opportunistic Multi-

Model Ensemble (MioMIP1), Paleoceanography and Paleoclimatology, 36, e2020PA004054, https://doi.org/10.1029/2020PA004054, 2021.

Butzin, M., Köhler, P., and Lohmann, G.: Marine radiocarbon reservoir age simulations for the past 50,000 years, Geophysical Research Letters, 44, 8473-8480, https://doi.org/10.1002/2017GL074688, 2017.

Cao, J.: NUIST NESMv3 model output prepared for CMIP6 PMIP midHolocene, Version 20190926, Earth System Grid Federation, https://doi.org/10.22033/ESGF/CMIP6.8773, 2019a.

Cao, J.: NUIST NESMv3 model output prepared for CMIP6 PMIP lig127k, Version 20190927, Earth System Grid Federation, https://doi.org/10.22033/ESGF/CMIP6.8772, 2019b.

Cao, J. and Wang, B.: NUIST NESMv3 model output prepared for CMIP6 CMIP piControl, Version 20190704, Earth System Grid Federation, https://doi.org/10.22033/ESGF/CMIP6.8776, 2019.

Cavagna, A. J., Dehairs, F., Bouillon, S., Woule-Ebongué, V., Planchon, F., Delille, B., and Bouloubassi, I.: Water column distribution and carbon isotopic signal of cholesterol, brassicasterol and particulate organic carbon in the Atlantic sector of the Southern Ocean, Biogeosciences, 10, 2787-2801, https://doi.org/10.5194/bg-10-2787-2013, 2013.

Crucifix, M., Braconnot, P., Harrison, S. P., and Otto-Bliesner, B.: Second phase of paleoclimate modelling intercomparison project, Eos, Transactions American Geophysical Union, 86, 264-264, https://doi.org/10.1029/2005EO280003, 2005.

Dallmeyer, A., Claussen, M., Wang, Y., and Herzschuh, U.: Spatial variability of Holocene changes in the annual precipitation pattern: a model-data synthesis for the Asian monsoon region, Climate Dynamics, 40, 2919-2936, https://doi.org/10.1007/s00382-012-1550-6, 2013.

Dallmeyer, A., Claussen, M., Fischer, N., Haberkorn, K., Wagner, S., Pfeiffer, M., Jin, L., Khon, V., Wang, Y., and Herzschuh, U.: The evolution of sub-monsoon systems in the Afro-Asian monsoon region during the Holocene– comparison of different transient climate model simulations, Clim. Past, 11, 305-326, https://doi.org/10.5194/cp-11-305-2015, 2015.

Danabasoglu, G.: NCAR CESM2-FV2 model output prepared for CMIP6 CMIP piControl, Version 20191120, Earth System Grid Federation, https://doi.org/10.22033/ESGF/CMIP6.11301, 2019a.

Danabasoglu, G.: NCAR CESM2-WACCM-FV2 model output prepared for CMIP6 CMIP piControl, Version 20191120, Earth System Grid Federation, https://doi.org/10.22033/ESGF/CMIP6.11302, 2019b.

Danabasoglu, G.: NCAR CESM2 model output prepared for CMIP6 PMIP midHolocene, Version 20190923, Earth System Grid Federation, https://doi.org/10.22033/ESGF/CMIP6.7674, 2019c.

Danabasoglu, G.: NCAR CESM2 model output prepared for CMIP6 PMIP lig127k, Version 20190923, Earth System Grid Federation, https://doi.org/10.22033/ESGF/CMIP6.7673, 2019d.

Danabasoglu, G., Lawrence, D., Lindsay, K., Lipscomb, W., and Strand, G.: NCAR CESM2 model output prepared for CMIP6 CMIP piControl. Version 20190320, Earth System Grid Federation, https://doi.org/10.22033/ESGF/CMIP6.7733, 2019.

Danek, C., Shi, X., Stepanek, C., Yang, H., Barbi, D., Hegewald, J., and Lohmann, G.: AWI AWI-ESM1.1LR model output prepared for CMIP6 CMIP piControl, Version 20200212, Earth System Grid Federation, https://doi.org/10.22033/ESGF/CMIP6.9335, 2020.

Earth Consortium: EC-Earth-Consortium EC-Earth3-LR model output prepared for CMIP6 CMIP piControl, Version 20200919, Earth System Grid Federation, https://doi.org/10.22033/ESGF/CMIP6.4847, 2019.

Earth Consortium: EC-Earth-Consortium EC-Earth3-LR model output prepared for CMIP6 PMIP midHolocene, Version 20200919, Earth System Grid Federation, https://doi.org/10.22033/ESGF/CMIP6.4801, 2020a.

Earth Consortium: EC-Earth-Consortium EC-Earth3-LR model output prepared for CMIP6 PMIP lig127k, Version 20200919, Earth System Grid Federation, https://doi.org/10.22033/ESGF/CMIP6.4798, 2020b.

Eyring, V., Bony, S., Meehl, G. A., Senior, C. A., Stevens, B., Stouffer, R. J., and Taylor, K. E.: Overview of the Coupled Model Intercomparison Project Phase 6 (CMIP6) experimental design and organization, Geosci. Model Dev., 9, 1937-1958, https://doi.org/10.5194/gmd-9-1937-2016, 2016.

Fietz, S., Ho, S. L., Huguet, C., Rosell-Melé, A., and Martínez-García, A.: Appraising GDGT-based seawater temperature indices in the Southern Ocean, Organic Geochemistry, 102, 93-105, https://doi.org/10.1016/j.orggeochem.2016.10.003, 2016.

Geibert, W., Stimac, I., Rutgers Van Der Loeff, M., and Kuhn, G.: Dating Deep-Sea Sediments With 230Th Excess Using a Constant Rate of Supply Model, Paleoceanography and Paleoclimatology, 34, 1895-1912, https://doi.org/10.1029/2019PA003663, 2019.

Gierz, P., Werner, M., and Lohmann, G.: Simulating climate and stable water isotopes during the Last Interglacial using a coupled climate-isotope model, Journal of Advances in Modeling Earth Systems, 9, 2027-2045, https://doi.org/10.1002/2017MS001056, 2017.

Guagnin, M., Jennings, R., Eager, H., Parton, A., Stimpson, C., Stepanek, C., Pfeiffer, M., Groucutt, H. S., Drake, N. A., Alsharekh, A., and Petraglia, M. D.: Rock art imagery as a proxy for Holocene environmental change: A view from Shuwaymis, NW Saudi Arabia, The Holocene, 26, 1822-1834, https://doi.org/10.1177/0959683616645949, 2016.

Guo, C., Bentsen, M., Bethke, I., Ilicak, M., Tjiputra, J., Toniazzo, T., Schwinger, J., and Otterå, O. H.: NCC NorESM1-F model output prepared for CMIP6 CMIP piControl, Version 20190920, Earth System Grid Federation, https://doi.org/10.22033/ESGF/CMIP6.11595, 2019a.

Guo, C., Bentsen, M., Bethke, I., Ilicak, M., Tjiputra, J., Toniazzo, T., Schwinger, J., and Otterå, O. H.: NCC NorESM1-F model output prepared for CMIP6 PMIP midHolocene, Version 20190920, Earth System Grid Federation, https://doi.org/10.22033/ESGF/CMIP6.11591, 2019b.

Guo, C., Bentsen, M., Bethke, I., Ilicak, M., Tjiputra, J., Toniazzo, T., Schwinger, J., and Otterå, O. H.: NCC NorESM1-F model output prepared for CMIP6 PMIP lig127k, Version 20190920, Earth System Grid Federation, https://doi.org/10.22033/ESGF/CMIP6.11590, 2019c.

Hajima, T., Abe, M., Arakawa, O., Suzuki, T., Komuro, Y., Ogura, T., Ogochi, K., Watanabe, M., Yamamoto, A., Tatebe, H., Noguchi, M. A., Ohgaito, R., Ito, A., Yamazaki, D., Ito, A., Takata, K., Watanabe, S., Kawamiya, M., and Tachiiri, K.: MIROC MIROC-ES2L model output prepared for CMIP6 CMIP piControl, Version 20190823, Earth System Grid Federation, https://doi.org/10.22033/ESGF/CMIP6.5710, 2019.

Haywood, A. M., Hill, D. J., Dolan, A. M., Otto-Bliesner, B. L., Bragg, F., Chan, W. L., Chandler, M. A., Contoux, C., Dowsett, H. J., Jost, A., Kamae, Y., Lohmann, G., Lunt, D. J., Abe-Ouchi, A., Pickering, S. J., Ramstein, G., Rosenbloom, N. A., Salzmann, U., Sohl, L., Stepanek, C., Ueda, H., Yan, Q., and Zhang, Z.: Large-scale features of Pliocene climate: results from the Pliocene Model Intercomparison Project, Clim. Past, 9, 191-209, https://doi.org/10.5194/cp-9-191-2013, 2013.

Haywood, A. M., Tindall, J. C., Dowsett, H. J., Dolan, A. M., Foley, K. M., Hunter, S. J., Hill, D. J., Chan, W. L., Abe-Ouchi, A., Stepanek, C., Lohmann, G., Chandan, D., Peltier, W. R., Tan, N., Contoux, C., Ramstein, G., Li, X., Zhang, Z., Guo, C., Nisancioglu, K. H., Zhang, Q., Li, Q., Kamae, Y., Chandler, M. A., Sohl, L. E., Otto-Bliesner, B. L., Feng, R., Brady, E. C., von der Heydt, A. S., Baatsen, M. L. J., and Lunt, D. J.: The Pliocene Model Intercomparison Project Phase 2: large-scale climate features and climate sensitivity, Clim. Past, 16, 2095-2123, https://doi.org/10.5194/cp-16-2095-2020, 2020.

Heaton, T. J., Köhler, P., Butzin, M., Bard, E., Reimer, R. W., Austin, W. E. N., Bronk Ramsey, C., Grootes, P. M., Hughen, K. A., Kromer, B., Reimer, P. J., Adkins, J., Burke, A., Cook, M. S., Olsen, J., and Skinner, L. C.: Marine20—The Marine Radiocarbon Age Calibration Curve (0–55,000 cal BP), Radiocarbon, 62, 779-820, https://doi.org/10.1017/RDC.2020.68, 2020.

Hopmans, E. C., Weijers, J. W. H., Schefuß, E., Herfort, L., Sinninghe Damsté, J. S., and Schouten, S.: A novel proxy for terrestrial organic matter in sediments based on branched and isoprenoid tetraether lipids, Earth and Planetary Science Letters, 224, 107-116, https://doi.org/10.1016/j.epsl.2004.05.012, 2004.

Hossain, A., Knorr, G., Jokat, W., and Lohmann, G.: Opening of the Fram Strait led to the establishment of a modern-like three-layer stratification in the Arctic Ocean during the Miocene, arktos, 7, 1-12, https://doi.org/10.1007/s41063-020-00079-8, 2021.

Hossain, A., Knorr, G., Lohmann, G., Stärz, M., and Jokat, W.: Simulated Thermohaline Fingerprints in Response to Different Greenland-Scotland Ridge and Fram Strait Subsidence Histories, Paleoceanography and Paleoclimatology, 35, e2019PA003842, https://doi.org/10.1029/2019PA003842, 2020.

Inglis, G. N., Farnsworth, A., Lunt, D., Foster, G. L., Hollis, C. J., Pagani, M., Jardine, P. E., Pearson, P. N., Markwick, P., Galsworthy, A. M. J., Raynham, L., Taylor, K. W. R., and Pancost, R. D.: Descent toward the Icehouse: Eocene sea surface cooling inferred from GDGT distributions, Paleoceanography, 30, 1000-1020, https://doi.org/10.1002/2014PA002723, 2015.

Jennings, R. P., Singarayer, J., Stone, E. J., Krebs-Kanzow, U., Khon, V., Nisancioglu, K. H., Pfeiffer, M., Zhang, X., Parker, A., Parton, A., Groucutt, H. S., White, T. S., Drake, N. A., and Petraglia, M. D.: The greening of Arabia: Multiple opportunities for human occupation of the Arabian Peninsula during the Late Pleistocene inferred from an ensemble of climate model simulations, Quaternary International, 382, 181-199, https://doi.org/10.1016/j.quaint.2015.01.006, 2015.

Jungclaus, J., Mikolajewicz, U., Kapsch, M.-L., D'Agostino, R., Wieners, K.-H., Giorgetta, M., Reick, C., Esch, M., Bittner, M., Legutke, S., Schupfner, M., Wachsmann, F., Gayler, V., Haak, H., de Vrese, P., Raddatz, T., Mauritsen, T., von Storch, J.-S., Behrens, J., Brovkin, V., Claussen, M., Crueger, T., Fast, I., Fiedler, S., Hagemann, S., Hohenegger, C., Jahns, T., Kloster, S., Kinne, S., Lasslop, G., Kornblueh, L., Marotzke, J., Matei, D., Meraner, K., Modali, K., Müller, W., Nabel, J., Notz, D., Peters-von Gehlen, K., Pincus, R., Pohlmann, H., Pongratz, J., Rast, S., Schmidt, H., Schnur, R., Schulzweida, U., Six, K., Stevens, B., Voigt, A., and Roeckner, E.: MPI-M MPI-ESM1.2-LR model output prepared for CMIP6 PMIP midHolocene, Version 20190710, Earth System Grid Federation, https://doi.org/10.22033/ESGF/CMIP6.6644, 2019a.

Jungclaus, J., Mikolajewicz, U., Kapsch, M.-L., D'Agostino, R., Wieners, K.-H., Giorgetta, M., Reick, C., Esch, M., Bittner, M., Legutke, S., Schupfner, M., Wachsmann, F., Gayler, V., Haak, H., de Vrese, P., Raddatz, T., Mauritsen, T., von Storch, J.-S., Behrens, J., Brovkin, V., Claussen, M., Crueger, T., Fast, I., Fiedler, S., Hagemann, S., Hohenegger, C., Jahns, T., Kloster, S., Kinne, S., Lasslop, G., Kornblueh, L., Marotzke, J., Matei, D., Meraner, K., Modali, K., Müller, W., Nabel, J., Notz, D., Peters-von Gehlen, K., Pincus, R., Pohlmann, H., Pongratz, J., Rast, S., Schmidt, H., Schnur, R., Schulzweida, U., Six, K., Stevens, B., Voigt, A., and Roeckner, E.: MPI-M MPI-ESM1.2-LR model output prepared for CMIP6 PMIP lgm, Version 20190710, Earth System Grid Federation, https://doi.org/10.22033/ESGF/CMIP6.6642, 2019b.

Kaboth-Bahr, S., Bahr, A., Stepanek, C., Catunda, M. C. A., Karas, C., Ziegler, M., García-Gallardo, Á., and Grunert, P.: Mediterranean heat injection to the North Atlantic delayed the intensification of Northern Hemisphere glaciations, Communications Earth & Environment, 2, 158, https://doi.org/10.1038/s43247-021-00232-5, 2021.

Kageyama, M., Albani, S., Braconnot, P., Harrison, S. P., Hopcroft, P. O., Ivanovic, R. F., Lambert, F., Marti, O., Peltier, W. R., Peterschmitt, J. Y., Roche, D. M., Tarasov, L., Zhang, X., Brady, E. C., Haywood, A. M., LeGrande, A. N., Lunt, D. J., Mahowald, N. M., Mikolajewicz, U., Nisancioglu, K. H., Otto-Bliesner, B. L., Renssen, H., Tomas, R. A., Zhang, Q., Abe-Ouchi, A., Bartlein, P. J., Cao, J., Li, Q., Lohmann, G., Ohgaito, R., Shi, X., Volodin, E., Yoshida, K., Zhang, X., and Zheng, W.: The

PMIP4 contribution to CMIP6 – Part 4: Scientific objectives and experimental design of the PMIP4-CMIP6 Last Glacial Maximum experiments and PMIP4 sensitivity experiments, Geosci. Model Dev., 10, 4035-4055, https://doi.org/10.5194/gmd-10-4035-2017, 2017.

Kim, J.-H., Schouten, S., Rodrigo-Gámiz, M., Rampen, S., Marino, G., Huguet, C., Helmke, P., Buscail, R., Hopmans, E. C., Pross, J., Sangiorgi, F., Middelburg, J. B. M., and Sinninghe Damsté, J. S.: Influence of deep-water derived isoprenoid tetraether lipids on the TEX86H paleothermometer in the Mediterranean Sea, Geochimica et Cosmochimica Acta, 150, 125-141, https://doi.org/10.1016/j.gca.2014.11.017, 2015.

Klages, J. P., Salzmann, U., Bickert, T., Hillenbrand, C.-D., Gohl, K., Kuhn, G., Bohaty, S. M., Titschack, J., Müller, J., Frederichs, T., Bauersachs, T., Ehrmann, W., van de Flierdt, T., Pereira, P. S., Larter, R. D., Lohmann, G., Niezgodzki, I., Uenzelmann-Neben, G., Zundel, M., Spiegel, C., Mark, C., Chew, D., Francis, J. E., Nehrke, G., Schwarz, F., Smith, J. A., Freudenthal, T., Esper, O., Pälike, H., Ronge, T. A., Dziadek, R., Afanasyeva, V., Arndt, J. E., Ebermann, B., Gebhardt, C., Hochmuth, K., Küssner, K., Najman, Y., Riefstahl, F., Scheinert, M., and the Science Team of Expedition, P. S.: Temperate rainforests near the South Pole during peak Cretaceous warmth, Nature, 580, 81-86, https://doi.org/10.1038/s41586-020-2148-5, 2020.

Knorr, G. and Lohmann, G.: Climate warming during Antarctic ice sheet expansion at the Middle Miocene transition, Nature Geoscience, 7, 376-381, https://doi.org/10.1038/ngeo2119, 2014.

Knorr, G., Butzin, M., Micheels, A., and Lohmann, G.: A warm Miocene climate at low atmospheric CO2 levels, Geophysical Research Letters, 38, https://doi.org/10.1029/2011GL048873, 2011.

Knorr, G., Barker, S., Zhang, X., Lohmann, G., Gong, X., Gierz, P., Stepanek, C., and Stap, L. B.: A salty deep ocean as a prerequisite for glacial termination, Nature Geoscience, 14, 930-936, https://doi.org/10.1038/s41561-021-00857-3, 2021.

Kotov, S. and Pälike, H.: QAnalySeries-a cross-platform time series tuning and analysis tool, AGU Fall Meeting Abstracts, PP53D-1230,

Langner, M. and Mulitza, S.: Technical note: PaleoDataView – a software toolbox for the collection, homogenization and visualization of marine proxy data, Clim. Past, 15, 2067-2072, https://doi.org/10.5194/cp-15-2067-2019, 2019.

Li, L.: CAS FGOALS-g3 model output prepared for CMIP6 CMIP piControl, Version 20191126, Earth System Grid Federation, https://doi.org/10.22033/ESGF/CMIP6.3448, 2019.

Lisiecki, L. E. and Raymo, M. E.: A Pliocene-Pleistocene stack of 57 globally distributed benthic δ18O records, Paleoceanography, 20, https://doi.org/10.1029/2004PA001071, 2005.

Lohmann, G., Knorr, G., Hossain, A., and Stepanek, C.: Effects of CO2 and Ocean Mixing on Miocene and Pliocene Temperature Gradients, Paleoceanography and Paleoclimatology, 37, e2020PA003953, https://doi.org/10.1029/2020PA003953, 2022.

Lunt, D. J., Abe-Ouchi, A., Bakker, P., Berger, A., Braconnot, P., Charbit, S., Fischer, N., Herold, N., Jungclaus, J. H., Khon, V. C., Krebs-Kanzow, U., Langebroek, P. M., Lohmann, G., Nisancioglu, K. H., Otto-Bliesner, B. L., Park, W., Pfeiffer, M., Phipps, S. J., Prange, M., Rachmayani, R., Renssen, H., Rosenbloom, N., Schneider, B., Stone, E. J., Takahashi, K., Wei, W., Yin, Q., and Zhang, Z. S.: A multi-model assessment of last interglacial temperatures, Clim. Past, 9, 699-717, https://doi.org/10.5194/cp-9-699-2013, 2013.

Lunt, D. J., Bragg, F., Chan, W. L., Hutchinson, D. K., Ladant, J. B., Morozova, P., Niezgodzki, I., Steinig, S., Zhang, Z., Zhu, J., Abe-Ouchi, A., Anagnostou, E., de Boer, A. M., Coxall, H. K., Donnadieu, Y., Foster, G., Inglis, G. N., Knorr, G., Langebroek, P. M., Lear, C. H., Lohmann, G., Poulsen, C. J., Sepulchre, P., Tierney, J. E., Valdes, P. J., Volodin, E. M., Dunkley Jones, T., Hollis, C. J., Huber, M., and Otto-Bliesner, B. L.: DeepMIP: model intercomparison of early Eocene climatic optimum (EECO) large-scale climate features and comparison with proxy data, Clim. Past, 17, 203-227, https://doi.org/10.5194/cp-17-203-2021, 2021.

Luo, F., Ying, J., Liu, T., and Chen, D.: Origins of Southern Ocean warm sea surface temperature bias in CMIP6 models, npj Climate and Atmospheric Science, 6, 127, https://doi.org/10.1038/s41612-023-00456-6, 2023.

Mollenhauer, G., Grotheer, H., Gentz, T., Bonk, E., and Hefter, J.: Standard operation procedures and performance of the MICADAS radiocarbon laboratory at Alfred Wegener Institute (AWI), Germany, Nuclear Instruments and Methods in Physics Research Section B: Beam Interactions with Materials and Atoms, 496, 45-51, https://doi.org/10.1016/j.nimb.2021.03.016, 2021.

NASA Goddard Institute for Space Studies: NASA-GISS GISS-E2.1G model output prepared for CMIP6 CMIP piControl, Version 20180824, Earth System Grid Federation, https://doi.org/10.22033/ESGF/CMIP6.7380, 2018.

NASA Goddard Institute for Space Studies: NASA-GISS GISS-E2.1G model output prepared for CMIP6 PMIP midHolocene, Version 20190916, Earth System Grid Federation, https://doi.org/10.22033/ESGF/CMIP6.7225, 2019.

Niezgodzki, I., Tyszka, J., Knorr, G., and Lohmann, G.: Was the Arctic Ocean ice free during the latest Cretaceous? The role of CO2 and gateway configurations, Global and Planetary Change, 177, 201-212, https://doi.org/10.1016/j.gloplacha.2019.03.011, 2019.

O'ishi, R., Abe-Ouchi, A., Ohgaito, R., Abe, M., Arakawa, O., Ogochi, K., Hajima, T., Watanabe, M., Yamamoto, A., Tatebe, H., Noguchi, M. A., Ito, A., Yamazaki, D., Ito, A., Takata, K., Watanabe, S., Kawamiya, M., and Tachiiri, K.: MIROC MIROC-ES2L model output prepared for CMIP6 PMIP lig127k, Version 20191118, Earth System Grid Federation, https://doi.org/10.22033/ESGF/CMIP6.5645, 2019.

Ohgaito, R., Abe-Ouchi, A., Abe, M., Arakawa, O., Ogochi, K., Hajima, T., Watanabe, M., Yamamoto, A., Tatebe, H., Noguchi, M. A., Ito, A., Yamazaki, D., Ito, A., Takata, K., Watanabe, S., Kawamiya, M., and Tachiiri, K.: MIROC MIROC-ES2L model output prepared for CMIP6 PMIP midHolocene, Version 20191002, Earth System Grid Federation, https://doi.org/10.22033/ESGF/CMIP6.5646., 2019a.

Ohgaito, R., Abe-Ouchi, A., Abe, M., Arakawa, O., Ogochi, K., Hajima, T., Watanabe, M., Yamamoto, A., Tatebe, H., Noguchi, M. A., Ito, A., Yamazaki, D., Ito, A., Takata, K., Watanabe, S., Kawamiya, M., and Tachiiri, K.: MIROC MIROC-ES2L model output prepared for CMIP6 PMIP lgm, Version 20191002, Earth System Grid Federation, https://doi.org/10.22033/ESGF/CMIP6.5644, 2019b.

Otto-Bliesner, B. L., Braconnot, P., Harrison, S. P., Lunt, D. J., Abe-Ouchi, A., Albani, S., Bartlein, P. J., Capron, E., Carlson, A. E., Dutton, A., Fischer, H., Goelzer, H., Govin, A., Haywood, A., Joos, F., LeGrande, A. N., Lipscomb, W. H., Lohmann, G., Mahowald, N., Nehrbass-Ahles, C., Pausata, F. S. R., Peterschmitt, J. Y., Phipps, S. J., Renssen, H., and Zhang, Q.: The PMIP4 contribution to CMIP6 – Part 2: Two interglacials, scientific objective and experimental design for Holocene and Last Interglacial simulations, Geosci. Model Dev., 10, 3979-4003, https://doi.org/10.5194/gmd-10-3979-2017, 2017.

Park, E.: Variations in GDGT flux and TEX86 thermometry in three distinct oceanic regimes of the Atlantic Ocean: a sediment trap study, University of Bremen, 2019.

Pfeiffer, M. and Lohmann, G.: Greenland Ice Sheet influence on Last Interglacial climate: global sensitivity studies performed with an atmosphere–ocean general circulation model, Clim. Past, 12, 1313-1338, https://doi.org/10.5194/cp-12-1313-2016, 2016.

Ridley, J., Menary, M., Kuhlbrodt, T., Andrews, M., and Andrews, T.: MOHC HadGEM3-GC31-LL model output prepared for CMIP6 CMIP piControl. Version 20211103, Earth System Grid Federation, https://doi.org/10.22033/ESGF/CMIP6.6294, 2018.

Schouten, S., Hopmans, E. C., and Damsté, J. S. S.: The organic geochemistry of glycerol dialkyl glycerol tetraether lipids: A review, Organic geochemistry, 54, 19-61, http://dx.doi.org/10.1016/j.orggeochem.2012.09.006, 2013.

Seland, Ø., Bentsen, M., Oliviè, D. J. L., Toniazzo, T., Gjermundsen, A., Graff, L. S., Debernard, J. B., Gupta, A. K., He, Y., Kirkevåg, A., Schwinger, J., Tjiputra, J., Aas, K. S., Bethke, I., Fan, Y., Griesfeller, J., Grini, A., Guo, C., Ilicak, M., Karset, I. H. H., Landgren, O. A., Liakka, J., Moseid, K. O., Nummelin, A., Spensberger, C., Tang, H., Zhang, Z., Heinze, C., Iversen, T., and Schulz, M.: NCC NorESM2-LM model output prepared for CMIP6 CMIP piControl, Version 20210118,, Earth System Grid Federation, https://doi.org/10.22033/ESGF/CMIP6.8217, 2019.

Shi, X., Yang, H., Danek, C., and Lohmann, G.: AWI AWI-ESM1.1LR model output prepared for CMIP6 PMIP lgm, Version 20200212, Earth System Grid Federation, https://doi.org/10.22033/ESGF/CMIP6.9330, 2020a.

Shi, X., Yang, H., Danek, C., and Lohmann, G.: AWI AWI-ESM1.1LR model output prepared for CMIP6 PMIP lig127k, Version 20200212, Earth System Grid Federation, https://doi.org/10.22033/ESGF/CMIP6.9331, 2020b.

Stein, R., Fahl, K., Gierz, P., Niessen, F., and Lohmann, G.: Arctic Ocean sea ice cover during the penultimate glacial and the last interglacial, Nature Communications, 8, 373, https://doi.org/10.1038/s41467-017-00552-1, 2017.

Stein, R., Fahl, K., Schreck, M., Knorr, G., Niessen, F., Forwick, M., Gebhardt, C., Jensen, L., Kaminski, M., Kopf, A., Matthiessen, J., Jokat, W., and Lohmann, G.: Evidence for ice-free summers in the late Miocene central Arctic Ocean, Nature Communications, 7, 11148, https://doi.org/10.1038/ncomms11148, 2016.

Stepanek, C. and Lohmann, G.: Modelling mid-Pliocene climate with COSMOS, Geosci. Model Dev., 5, 1221-1243, https://doi.org/10.5194/gmd-5-1221-2012, 2012.

Stepanek, C., Samakinwa, E., Knorr, G., and Lohmann, G.: Contribution of the coupled atmosphere–ocean–sea ice–vegetation model COSMOS to the PlioMIP2, Clim. Past, 16, 2275-2323, https://doi.org/10.5194/cp-16-2275-2020, 2020.

Taylor, K. W. R., Huber, M., Hollis, C. J., Hernandez-Sanchez, M. T., and Pancost, R. D.: Re-evaluating modern and Palaeogene GDGT distributions: Implications for SST reconstructions, Global and Planetary Change, 108, 158-174, https://doi.org/10.1016/j.gloplacha.2013.06.011, 2013.

Varma, V., Prange, M., Merkel, U., Kleinen, T., Lohmann, G., Pfeiffer, M., Renssen, H., Wagner, A., Wagner, S., and Schulz, M.: Holocene evolution of the Southern Hemisphere westerly winds in transient simulations with global climate models, Clim. Past, 8, 391-402, https://doi.org/10.5194/cp-8-391-2012, 2012.

Voldoire, A.: CMIP6 simulations of the CNRM-CERFACS based on CNRM-CM6-1 model for CMIP experiment piControl, Version 20180814, Earth System Grid Federation, https://doi.org/10.22033/ESGF/CMIP6.4163, 2018.

Voldoire, A.: CNRM-CERFACS CNRM-CM6-1 model output prepared for CMIP6 PMIP lig127k, Version 20200212, Earth System Grid Federation, https://doi.org/10.22033/ESGF/CMIP6.4118, 2020.

Volodin, E., Mortikov, E., Gritsun, A., Lykossov, V., Galin, V., Diansky, N., Gusev, A., Kostrykin, S., Iakovlev, N., Shestakova, A., and Emelina, S.: INM INM-CM4-8 model output prepared for CMIP6 CMIP piControl. Version 20190605, Earth System Grid Federation, https://doi.org/10.22033/ESGF/CMIP6.5080, 2019a.

Volodin, E., Mortikov, E., Gritsun, A., Lykossov, V., Galin, V., Diansky, N., Gusev, A., Kostrykin, S., Iakovlev, N., Shestakova, A., and Emelina, S.: INM INM-CM4-8 model output prepared for CMIP6 PMIP midHolocene. Version 20190802, Earth System Grid Federation, https://doi.org/10.22033/ESGF/CMIP6.5077, 2019b.

Volodin, E., Mortikov, E., Gritsun, A., Lykossov, V., Galin, V., Diansky, N., Gusev, A., Kostrykin, S., Iakovlev, N., Shestakova, A., and Emelina, S.: INM INM-CM4-8 model output prepared for CMIP6

PMIP lgm, Version 20201112, Earth System Grid Federation, https://doi.org/10.22033/ESGF/CMIP6.5075, 2019c.

Weber, M. E., Bailey, I., Hemming, S. R., Martos, Y. M., Reilly, B. T., Ronge, T. A., Brachfeld, S., Williams, T., Raymo, M., Belt, S. T., Smik, L., Vogel, H., Peck, V. L., Armbrecht, L., Cage, A., Cardillo, F. G., Du, Z., Fauth, G., Fogwill, C. J., Garcia, M., Garnsworthy, M., Glüder, A., Guitard, M., Gutjahr, M., Hernández-Almeida, I., Hoem, F. S., Hwang, J.-H., Iizuka, M., Kato, Y., Kenlee, B., Oconnell, S., Pérez, L. F., Seki, O., Stevens, L., Tauxe, L., Tripathi, S., Warnock, J., and Zheng, X.: Antiphased dust deposition and productivity in the Antarctic Zone over 1.5 million years, Nature Communications, 13, 2044, https://doi.org/10.1038/s41467-022-29642-5, 2022.

Wei, W. and Lohmann, G.: Simulated Atlantic Multidecadal Oscillation during the Holocene, Journal of Climate, 25, 6989-7002, https://doi.org/10.1175/JCLI-D-11-00667.1, 2012.

Weijers, J. W. H., Schouten, S., Spaargaren, O. C., and Sinninghe Damsté, J. S.: Occurrence and distribution of tetraether membrane lipids in soils: Implications for the use of the TEX86 proxy and the BIT index, Organic Geochemistry, 37, 1680-1693, https://doi.org/10.1016/j.orggeochem.2006.07.018, 2006.

Wieners, K.-H., Giorgetta, M., Jungclaus, J., Reick, C., Esch, M., Bittner, M., Legutke, S., Schupfner, M., Wachsmann, F., Gayler, V., Haak, H., de Vrese, P., Raddatz, T., Mauritsen, T., von Storch, J.-S., Behrens, J., Brovkin, V., Claussen, M., Crueger, T., Fast, I., Fiedler, S., Hagemann, S., Hohenegger, C., Jahns, T., Kloster, S., Kinne, S., Lasslop, G., Kornblueh, L., Marotzke, J., Matei, D., Meraner, K., Mikolajewicz, U., Modali, K., Müller, W., Nabel, J., Notz, D., Peters-von Gehlen, K., Pincus, R., Pohlmann, H., Pongratz, J., Rast, S., Schmidt, H., Schnur, R., Schulzweida, U., Six, K., Stevens, B., Voigt, A., and Roeckner, E.: MPI-M MPI-ESM1.2-LR model output prepared for CMIP6 CMIP piControl, Version 20190710, Earth System Grid Federation, https://doi.org/10.22033/ESGF/CMIP6.6675, 2019.

Williams, C., Lunt, D., Singarayer, J., and Guarino, M. V.: NERC HadGEM3-GC31-LL model output prepared for CMIP6 PMIP midHolocene, Version 20210111, Earth System Grid Federation, https://doi.org/10.22033/ESGF/CMIP6.12129, 2021a.

Williams, C., Lunt, D., Singarayer, J., and Guarino, M. V.: NERC HadGEM3-GC31-LL model output prepared for CMIP6 PMIP lig127k, Version 20210114, Earth System Grid Federation, https://doi.org/10.22033/ESGF/CMIP6.12128, 2021b.

Yeung, N., Menviel, L., Meissner, K., Ziehn, T., Chamberlain, M., Mackallah, C., Druken, K., and Ridzwan, S., M.: CSIRO ACCESS-ESM1.5 model output prepared for CMIP6 PMIP lig127k, Version 20200817, Earth System Grid Federation, https://doi.org/10.22033/ESGF/CMIP6.13703, 2019.

Yu, Y.: CAS FGOALS-f3-L model output prepared for CMIP6 CMIP piControl, Version 20191028, Earth System Grid Federation, https://doi.org/10.22033/ESGF/CMIP6.3447, 2019.

Yukimoto, S., Koshiro, T., Kawai, H., Oshima, N., Yoshida, K., Urakawa, S., Tsujino, H., Deushi, M., Tanaka, T., Hosaka, M., Yoshimura, H., Shindo, E., Mizuta, R., Ishii, M., Obata, A., and Adachi, Y.: MRI MRI-ESM2.0 model output prepared for CMIP6 CMIP piControl, Version 20190904, Earth System Grid Federation, https://doi.org/10.22033/ESGF/CMIP6.6900, 2019a.

Yukimoto, S., Koshiro, T., Kawai, H., Oshima, N., Yoshida, K., Urakawa, S., Tsujino, H., Deushi, M., Tanaka, T., Hosaka, M., Yoshimura, H., Shindo, E., Mizuta, R., Ishii, M., Obata, A., and Adachi, Y.: MRI MRI-ESM2.0 model output prepared for CMIP6 PMIP midHolocene, Version 20190919, Earth System Grid Federation, https://doi.org/10.22033/ESGF/CMIP6.6860, 2019b.

Zhang, X., Lohmann, G., Knorr, G., and Xu, X.: Different ocean states and transient characteristics in Last Glacial Maximum simulations and implications for deglaciation, Clim. Past, 9, 2319-2333, https://doi.org/10.5194/cp-9-2319-2013, 2013.

Zhang, X., Barker, S., Knorr, G., Lohmann, G., Drysdale, R., Sun, Y., Hodell, D., and Chen, F.: Direct astronomical influence on abrupt climate variability, Nature Geoscience, 14, 819-826, https://doi.org/10.1038/s41561-021-00846-6, 2021.

Zhang, Y. G., Pagani, M., and Wang, Z.: Ring Index: A new strategy to evaluate the integrity of TEX86 paleothermometry, Paleoceanography, 31, 220-232, https://doi.org/10.1002/2015PA002848, 2016.

Zhang, Z., Bentsen, M., Oliviè, D. J. L., Seland, Ø., Toniazzo, T., Gjermundsen, A., Graff, L. S., Debernard, J. B., Gupta, A. K., He, Y., Kirkevåg, A., Schwinger, J., Tjiputra, J., Aas, K. S., Bethke, I., Fan, Y., Griesfeller, J., Grini, A., Guo, C., Ilicak, M., Karset, I. H. H., Landgren, O. A., Liakka, J., Moseid, K. O., Nummelin, A., Spensberger, C., Tang, H., Heinze, C., Iversen, T., and Schulz, M.: NCC NorESM2-LM model output prepared for CMIP6 PMIP midHolocene, Version 20191108, Earth System Grid Federation, https://doi.org/10.22033/ESGF/CMIP6.8079, 2019a.

Zhang, Z., Bentsen, M., Oliviè, D. J. L., Seland, Ø., Toniazzo, T., Gjermundsen, A., Graff, L. S., Debernard, J. B., Gupta, A. K., He, Y., Kirkevåg, A., Schwinger, J., Tjiputra, J., Aas, K. S., Bethke, I., Fan, Y., Griesfeller, J., Grini, A., Guo, C., Ilicak, M., Karset, I. H. H., Landgren, O. A., Liakka, J., Moseid, K. O., Nummelin, A., Spensberger, C., Tang, H., Heinze, C., Iversen, T., and Schulz, M.: NCC NorESM2-LM model output prepared for CMIP6 PMIP lig127k, Version 20191108, Earth System Grid Federation, https://doi.org/10.22033/ESGF/CMIP6.8078, 2019b.

Zheng, W. and Dong, L.: CAS FGOALS-g3 model output prepared for CMIP6 PMIP midHolocene, Version 20191026, Earth System Grid Federation, https://doi.org/10.22033/ESGF/CMIP6.3409, 2019a.

Zheng, W. and Dong, L.: CAS FGOALS-g3 model output prepared for CMIP6 PMIP lig127k, Version 20191030, Earth System Grid Federation, https://doi.org/10.22033/ESGF/CMIP6.3407, 2019b.

Zheng, W. and He, B.: CAS FGOALS-f3-L model output prepared for CMIP6 PMIP midHolocene, Version 20191101, Earth System Grid Federation, https://doi.org/10.22033/ESGF/CMIP6.12014, 2019a.

Zheng, W. and He, B.: CAS FGOALS-f3-L model output prepared for CMIP6 PMIP lig127k, Version 20191101, Earth System Grid Federation, https://doi.org/10.22033/ESGF/CMIP6.12013, 2019b.

Ziehn, T., Chamberlain, M., Lenton, A., Law, R., Bodman, R., Dix, M., Wang, Y., Dobrohotoff, P., Srbinovsky, J., Stevens, L., Vohralik, P., Mackallah, C., Sullivan, A., O'Farrell, S., and Druken, K.: CSIRO ACCESS-ESM1.5 model output prepared for CMIP6 CMIP piControl, Version 20210316, Earth System Grid Federation, https://doi.org/10.22033/ESGF/CMIP6.4312, 2019.

Zielinski, U., Bianchi, C., Gersonde, R., and Kunz-Pirrung, M.: Last occurrence datums of the diatoms Rouxia leventerae and Rouxia constricta: indicators for marine isotope stages 6 and 8 in Southern Ocean sediments, Marine Micropaleontology, 46, 127-137, https://doi.org/10.1016/S0377-8398(02)00042-7, 2002.